Wiley
Journal of GeoEnergy
Volume 2025, Article ID 4610521, 26 pages
https://doi.org/10.1155/jge5/4610521

Research Article

Screening Assessment of the Impact of Structural and Sedimentary Geological Heterogeneities on the Performance of an Ultra-Deep Carbonate Reservoir, North-Central Tarim Basin, Northwest China

Xinyu Dong,[1,2] Gary J. Hampson,[2] Carl Jacquemyn,[2] Matthew D. Jackson,[2] Dmytro Petrovskyy,[2,3] Sebastian Geiger,[3] and Yanghua Wang[1,2]

[1]*Resource Geophysics Academy, Department of Earth Science and Engineering, Imperial College London, South Kensington, London, SW7 2BP, UK*
[2]*Department of Earth Science and Engineering, Imperial College London, South Kensington, London, SW7 2AZ, UK*
[3]*Department of Geoscience and Engineering, Delft University of Technology, Delft 2600 AA, Netherlands*

Correspondence should be addressed to Gary J. Hampson; g.j.hampson@imperial.ac.uk

Received 14 February 2025; Accepted 16 April 2025

Academic Editor: Sun Mengdi

Carbonate reservoirs host significant hydrocarbon, groundwater, geothermal and CO_2- and H_2-storage resources. However, their complex depositional, tectonic and diagenetic histories make it challenging to efficiently characterize and predict their flow behavior. Here, we use a novel, rapid and efficient screening methodology that integrates experimental design, the construction of three-dimensional (3D) reservoir models via sketch-based methods and single-phase flow diagnostics to investigate the impact of geological heterogeneity on flow patterns and displacement in an ultra-deep (>7 km) carbonate reservoir in the north-central Tarim Basin, northwest China. Eight heterogeneities are investigated: (1) strike-slip fault zone width; (2) complexity of flower structure configuration; (3) continuity of fault core lithology; fault zone rock properties related to (4) karstification and (5) late, post-karstification cementation; (6) the occurrence of fault-perpendicular fracture corridors; (7) connectivity of fracture corridors to fault zones and (8) variability in host rock porosity and permeability. Fault zone width has the most significant impact on reservoir properties, with wider fault zones increasing effective horizontal permeability along fault zone strike. Fracture corridor occurrence and connectivity to the fault zone are the principal heterogeneities controlling effective permeability perpendicular to fault zone strike. Fault zone rock properties reflecting karstification and late cementation also significantly impact effective permeability in all directions. Other heterogeneities have little effect on effective permeability and well performance. However, simulated wells in negative flower structures and the main fault zone have higher productivities on average than simulated wells in positive flower structures and the host rock, similar to published production data from the ultra-deep reservoir. This study demonstrates the value of the screening methodology for assessing the effects of uncertainty in the interpretation of geological heterogeneities in complex carbonate reservoirs, in order to narrow the focus of future, more comprehensive reservoir simulations. The screening methodology is directly transferable to low-carbon energy applications in settings with sparse data.

1. Introduction

Carbonate formations host critical subsurface resources, including groundwater [1], geothermal energy [2] and hydrocarbons [3], and are potentially important storage units of CO_2 and H_2 [4]. Many carbonate formations contain complex geological heterogeneities (e.g., faults and fractures, karst and caves) that are notoriously difficult to characterize and model but are known to impact flow negatively [3, 5–7]. Sparse data compound the difficulty of characterizing and modeling such carbonate reservoirs [6].

One example of highly heterogeneous carbonate reservoirs in which production data illustrate variable flow patterns is provided by ultra-deep reservoirs, with burial depths >7000 m, in Ordovician strata of the Tarim Basin, northwest China. These ultra-deep carbonate reservoirs are characterized by tight host rocks (porosity <2%, permeability <5 mD) [8–12] which contain fractures and dissolution cavities that contribute secondary porosity [13–15]. The large burial depth of the reservoirs limits seismic resolution and the number and coverage of well penetrations, such that there is significant uncertainty in reservoir character and in identification of the most influential geological heterogeneities for fluid flow. Consequently, modeling and predicting the performance of these ultra-deep carbonate reservoirs is a significant challenge [12]. Previous studies have focussed on characterizing fault and karst distribution using seismic attribute analysis, well data and outcrop analogs [16–18], and generating reservoir models conditioned to seismic attribute and well data using discrete fracture network [19], geostatistical [20] and machine-learning approaches [21]. These latter approaches to reservoir modeling make *a priori* assumptions about the geological heterogeneities that control reservoir performance and may underrepresent uncertainty in reservoir character due to additional heterogeneites, particularly where data are sparse.

In this article, we address the potential limitations of previous reservoir characterization and modeling work by applying a rapid screening methodology to identify the key geological heterogeneities that control flow and production from one example of an ultra-deep, Middle Ordovician carbonate reservoir in the north-central Tarim Basin. The screening methodology combines experimental design, sketch-based reservoir modeling and flow diagnostics. Reservoir models are generic prototypes constructed using a sketch-based approach implemented in Open Source research code (Rapid Reservoir Modeling [RRM]), which has allowed scenarios for multiple types of geological heterogeneity to be modeled quickly in a geologically intuitive manner [22, 23]. Scenarios are based on published descriptions, interpretations, and conceptual models of ultra deep carbonate reservoirs in the north-central Tarim Basin. Our aim is to test the suitability of the sketch-based approach for modeling geometrically complex heterogeneities in carbonate reservoirs. The published production data from the reservoir are then used to test and calibrate the sketch-based models via computationally efficient flow diagnostics [24]. Although the data for this case study comes from a hydrocarbon field, the proposed workflow is relevant for a wide range of energy transition applications. For example, the unexpected presence of fracture corridors in carbonate formations hosting a deep geothermal reservoir in the vicinity of Munich, Germany, has led to a premature breakthrough of cold water that impacts the economic viability of the geothermal project [25, 26]. Similarly, understanding the geometry of faults and fault properties is crucial to quantifying the economic viability of a geothermal system [27] and ensuring that leakage during CO_2 storage projects can be derisked [28]. Many low-carbon energy applications, such as CO_2 storage or geothermal energy take place in data-poor environments, not dissimilar to the situation encountered in this case study from the Tarim Basin. Hence, these applications require fast and efficient screening methods that allow a range of geological scenarios to be explored as a preliminary step before commencing on more detailed modeling and flow simulation [29, 30].

2. Geological Setting

2.1. Tectonic, Stratigraphic, and Petroleum System Context. The Tarim Basin, situated in northwest China and covering an area of approximately $5.6 \times 10^5\,km^2$, is bounded by the Tianshan Mountains to the north, the Altyn Mountains to the east and the Kunlun Mountains to the south (Figure 1) [34]. This basin has a complex, polyphase evolutionary history that includes Proterozoic to Middle Silurian extension, Late Silurian compression, Carboniferous to Middle Triassic extension, Late Triassic compression, Jurassic to Paleogene extension and Neogene compression [8, 34, 35]. It comprises 11 tectonic elements, commonly referred to in published literature as 'depressions' and 'uplifts', based on their stratal and structural characteristics (Figure 1) [31, 36]. The basin features Proterozoic (Pre-Sinian) metamorphic basement [34], and its basin-fill strata include Late Precambrian (Sinian) to Paleozoic marine carbonates, Mesozoic marine and continental siliciclastic strata and Cenozoic continental siliciclastic strata (Figure 2) [8]. In the Early Permian, large igneous province magmatism occurred in the Tarim Basin [39, 40], which is inferred to have driven large-scale circulation of hydrothermal fluids [41, 42].

Thick (~3 km) and widespread ($4 \times 10^5\,km^2$) Early Cambrian to Middle Cambrian and Ordovician limestones and dolomites (Qiulitagexia, Penglaiba, Yingshan, Yijianfang, Qiaerbake and Lianglitage formations; Figure 2) constitute the primary reservoir interval in the north-central Tarim Basin [43–45]. These strata document the establishment and persistence of a seismically imaged, long-lived carbonate platform with steeply dipping margins [34, 46]. Overlying Upper Ordovician mudstones (Sangtamu Formation; Figure 2) cap the reservoir interval and form a regional seal [12, 47, 48]. Outcrops along the northwestern basin margin and well penetrations within the basin indicate the development of reef–shoal complexes at multiple, laterally continuous stratigraphic levels within the strata of the Ordovician carbonate platform [46, 49].

The studied reservoir is located within the Shuntuoguole low uplift in the north-central Tarim basin (Figure 1) and is primarily developed in Early to Middle Ordovician carbonate strata (Yingshan and Yijianfang formations; Figure 2). These strata are buried at depths ranging from 7300 to 8500 m. The region surrounding the reservoir contains 18 main strike-slip fault zones that control the distribution of hydrocarbon accumulations (Figure 1C) [8, 31]. Moreover, carbonate strata in the central Tarim basin have experienced multiple stages of diagenetic alteration, impacting reservoir development beyond the heterogeneities caused by fault systems [10, 20]. The Cambrian shales to the east in the Manjiaer depression are identified as the primary source rocks for the Ordovician reservoirs in the study area [37, 50]. The SB1 fault, which traverses nearly the entire Paleozoic sequence,

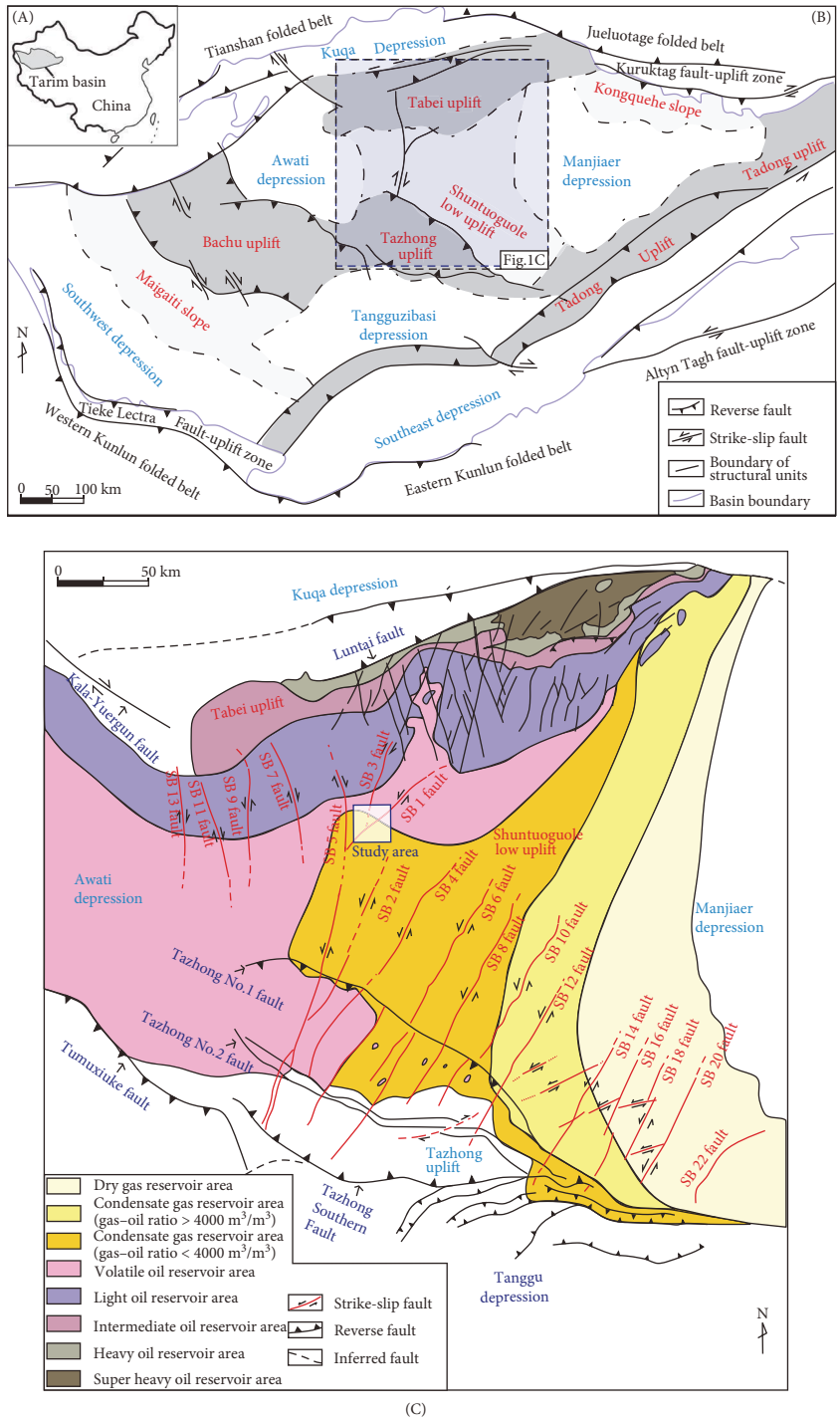

FIGURE 1: Maps locating the study area: (A) location of the Tarim Basin within China, (B) simplified tectonic map of the Tarim Basin (modified after [31, 32]) and (C) distribution of hydrocarbon phases in reservoir strata of the north-central Tarim Basin, with the inset box indicating the study area (modified after [12, 33]).

was variably active between the Late Ordovician and Early Permian [12, 31]. This fault and its related fracture network provided migration pathways for hydrocarbons from the Cambrian source rocks to the Ordovician reservoirs [8, 51].

2.2. Reservoir Stratigraphy. The studied reservoir was deposited in the interior of the Early to Middle Ordovician carbonate platform and comprises the Yingshan and Yijianfang formations (Figure 2) [38]. The Penglaiba and lower Yingshan formations predominantly consist of dolomites with interlayered chert [52]. In contrast, the upper Yingshan Formation consists mainly of carbonate grainstone, wackestone and mudstone. The Yijianfang Formation, comprising carbonate mudstone, intraclast grainstone, packstone and

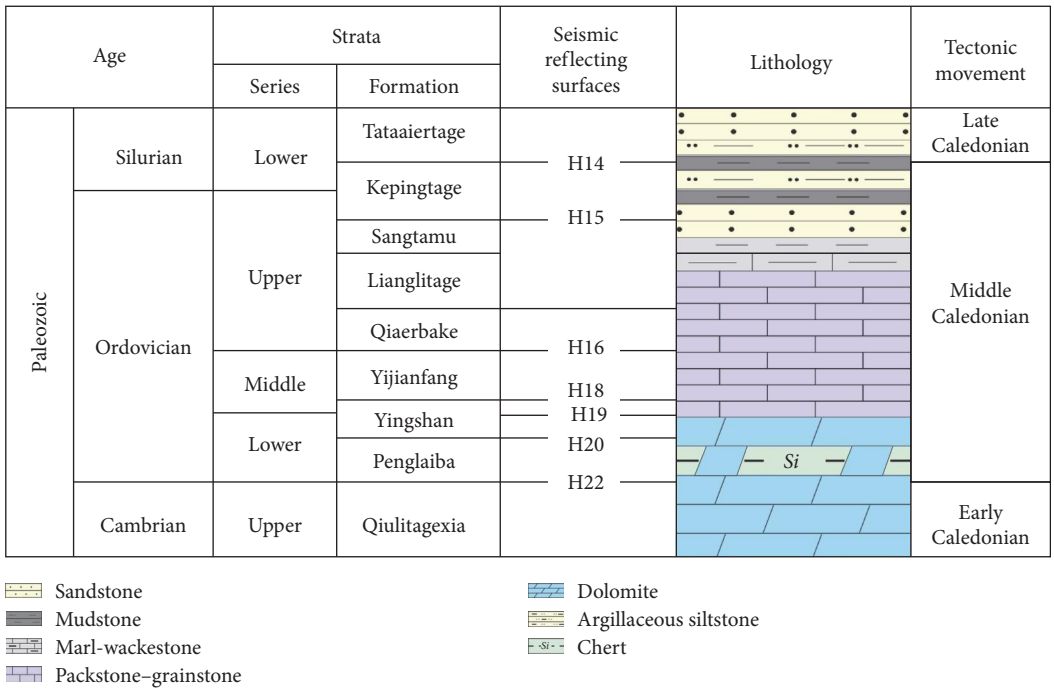

FIGURE 2: Stratigraphic column of Late Cambrian to Early Silurian formations in the study area (modified after [36, 37]). Mapped seismic reflectors of Dong et al. [38] and regional tectonic context are shown (modified after [8, 31, 36]).

wackestone, conformably overlies the upper Yingshan Formation [53]. These reservoir strata are characterized by generally continuous, subparallel seismic reflections [38]. Detailed seismic mapping and seismic facies analysis of the Penglaiba, Yingshan and Yijianfang formations reveals vertically stacked, sub-circular mounded structures that are 900–1200 m in diameter; these structures have not yet been penetrated by wells and are interpreted as composite reef–shoal complexes with an unknown diagenetic overprint [38]. In the studied field, the Qiaerbake Formation is characterized by carbonate mudstone, transitioning into thin layered carbonates and marl in the Lianglitage and Sangtamu formations, respectively [31, 54].

2.3. Fault Systems in the Reservoir. Strike-slip faults in the north-central Tarim Basin (Figure 1C) primarily developed during the Late Ordovician period but were reactivated in the Late Silurian to Early Devonian and in the Late Carboniferous to Early Permian [12, 31]. The faults penetrate Precambrian basement and extend through the reservoir and upward into Permian strata [32, 51]. Reservoir distribution and hydrocarbon accumulation occur predominantly along these deep-seated strike-slip faults [12, 31, 32, 55–57], with reservoir quality enhanced by hypogenic karstification due to the migration of hydrothermal fluids [8]. Fault-related karst reservoirs are developed along individual segments of the strike-slip faults, and reservoirs in different fault segments are not connected [10]. In the deep and ultra-deep carbonate reservoirs of the north-central Tarim Basin, highly productive wells are often located within 800 m of the core of strike-slip faults [58–60]. The studied reservoir is situated along the southwest-northeast-oriented SB1 fault (Figures 1C and 3). The fault displays left-lateral strike-slip offset and is marked by distinct negative (extensional) flower structure, vertical transition and positive (compressional) flower structure segments that are several kilometers in along-strike length in Middle Ordovician strata [10, 31, 51, 61, 62]. The segments of the SB1 fault, and other strike-slip faults, are interpreted to vary markedly in their structural characteristics [10]. Wells in the northern segments of the SB1 fault are significantly more productive than in the southern segments [62]. Furthermore, the negative flower structure segments of the SB1 fault show a higher degree of hydrocarbon accumulation than the positive flower structure and vertical transition segments [31]. Physical experiments suggest that increased intensity and extent of fault activity in both negative and positive flower structure segments generated densely fractured regions, with more widespread and connected fracture-related cavities occurring in the former than the latter [63].

2.4. Diagenetic Effects on Reservoir Quality. The deeply buried Ordovician carbonates in the studied reservoir are characterized by very low host rock porosity (<2%) and permeability (<5 mD) (Figure 4A,B) [10, 11]. However, hydrothermal activity and associated diagenesis have locally modified carbonate reservoir quality [33, 42, 64, 65]. Permian magmatism is considered to have generated hydrothermal fluids that migrated along faults and fractures, leading to the formation of hypogenic karst [11]. Additionally, deep hydrothermal karstification in the studied reservoir was also influenced by acidic fluids during Middle–Late Silurian and Devonian–Permian hydrocarbon generation and maturation episodes, as well as magnesium-rich fluid migration during Jurassic-Cretaceous deformation [66]. Hydrothermal fluids locally enhanced porosity by dissolving dolomite to create intercrystalline pores

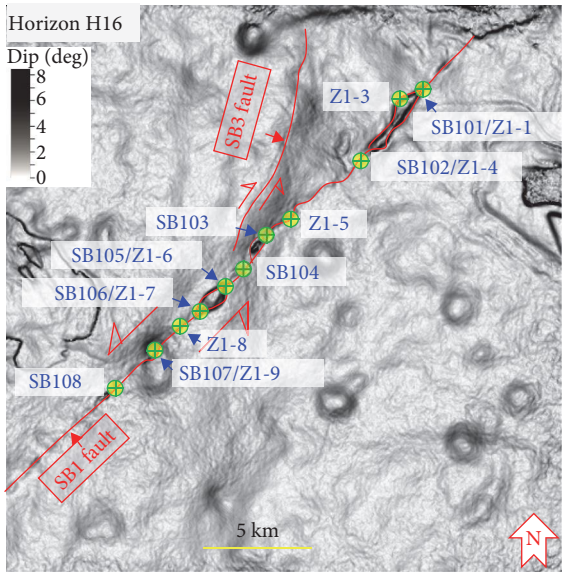

FIGURE 3: Dip attribute map of seismically mapped top-reservoir horizon H16 (Figure 2) in the study area (Figure 1C), showing strike-slip faults SB1 and SB3 and their constituent negative flower structure, transition and positive flower structure segments (after [10, 31, 51]). The map indicates the approximate location of wells with published production data (cf., wells Z1-1, Z1-3, Z1-4, Z1-5, Z1-6, Z1-7, Z1-8 and Z1-9 [10]; wells SHB101, SHB102, SHB103, SHB104, SHB105, SHB106, SHB107 and SHB108 [31]), and outlines the area of the reservoir comparable to the models used in this study.

and larger vugs (Figure 4C) [41, 67, 68], but decreased porosity through calcite, dolomite, fluorite and quartz cementation [52, 68, 69]. Multistage fracture diagenesis, particularly late-stage fracturing and fracture-related hydrothermal dissolution along fault and fracture zones, has also contributed to increased local porosity and permeability in the carbonate reservoirs of the Tarim Basin [9, 70].

3. Methodology

Our screening methodology follows that of Jackson et al. [29] and Alshakri et al. [30] and integrates three components: first, an experimental design that facilitates the systematic and efficient exploration of a wide range of parameters while requiring only a small number of models; second, a sketch-based reservoir modeling tool that enables the rapid construction of deterministic models; and third, single-phase flow diagnostics that provide computationally inexpensive approximations of more comprehensive, multiphase flow simulations. Each of these three components is described in more detail below.

3.1. Design of Modeling Experiment. We identified eight heterogeneities for detailed investigation (Table 1). Utilizing established experimental design methods [71–73], we adopted a two-level fractional-factorial design (2_{IV}^{8-3}) in which each heterogeneity is allocated a low or high setting (Table 1). This design uses 32 models (Table 2) to efficiently measure the impact of variance of each heterogeneity from its low to its high setting, while preventing these main effects from being confounded with two-factor interactions [71]. The 32 models enable ranking of the heterogeneities based on the average response of a given metric across the model ensemble.

3.2. Modeled Heterogeneities and Settings. The eight heterogeneities investigated in this study (Table 1) are described below in hierarchical order (Figure 5), at progressively smaller length scales. These eight heterogeneities are represented in models that share a common template, which is based on the structure of the SB1 fault in the study area (Figure 4). Each model contains a central strike-slip fault surrounded by host rock (Figures 6 and 7). The central strike-slip fault is divided into a positive flower structure segment, a vertical transition segment and a negative flower structure segment. Each model represents a volume of 6 km (x, parallel to fault strike) × 3 km (y, perpendicular to fault strike) × 1.76 km (z) (Figure 6).

3.2.1. Fault Zone Width. In the north-central Tarim basin, the width of strike-slip fault zones varies considerably between different fault segments, typically ranging from 100 to 800 m [60, 61]. Fault zones contain a narrow, central fault core and a broader, outer fault damage zone, including those within the studied reservoir [74]. The fault core contains high-strain products (e.g., gouge, breccia, cataclasite, ultracataclasite) that generally exhibit lower permeability than other parts of the fault system [75–77]. The damage zone consists of fractured host rock and cataclasite and lies on either side of the fault core. Dense fractures within the damage zone may lead to relatively high permeability [77–79], facilitating fluid migration and enhancing karstification and dolomitization processes [32, 80, 81]. Fault zone width may significantly influence reservoir properties, as a broader fault damage zone often correlates with a wider zone of high permeability [82, 83]. For simplicity, fault zones are represented in our models as having a uniform width, with damage zones located symmetrically on either side of the fault core (Figures 6 and 7). The high setting of fault zone width is 600 m, comprising a 200 m wide core and 200 m wide damage zones, whereas the low setting is 180 m, comprising a 60 m wide core and 60 m wide damage zones (Table 1).

3.2.2. Complexity of Flower Structure Configuration. Positive and negative flower structure segments of strike-slip faults Deleted are structurally complex and typically contain additional, secondary faults. Negative flower structures are characterized by a shallow synform bounded by strands of a strike-slip fault that spread upward, exhibiting primarily normal separations [84]. Positive flower structures feature a shallow antiform displaced by upward-diverging strands of a strike-slip fault, with predominantly reverse separations [84]. Three orders of secondary faults are identified within positive flower structures in the study area: the first order as NE-SW-oriented boundary faults and the second and third orders presenting a variety of orientations [51, 61, 85].

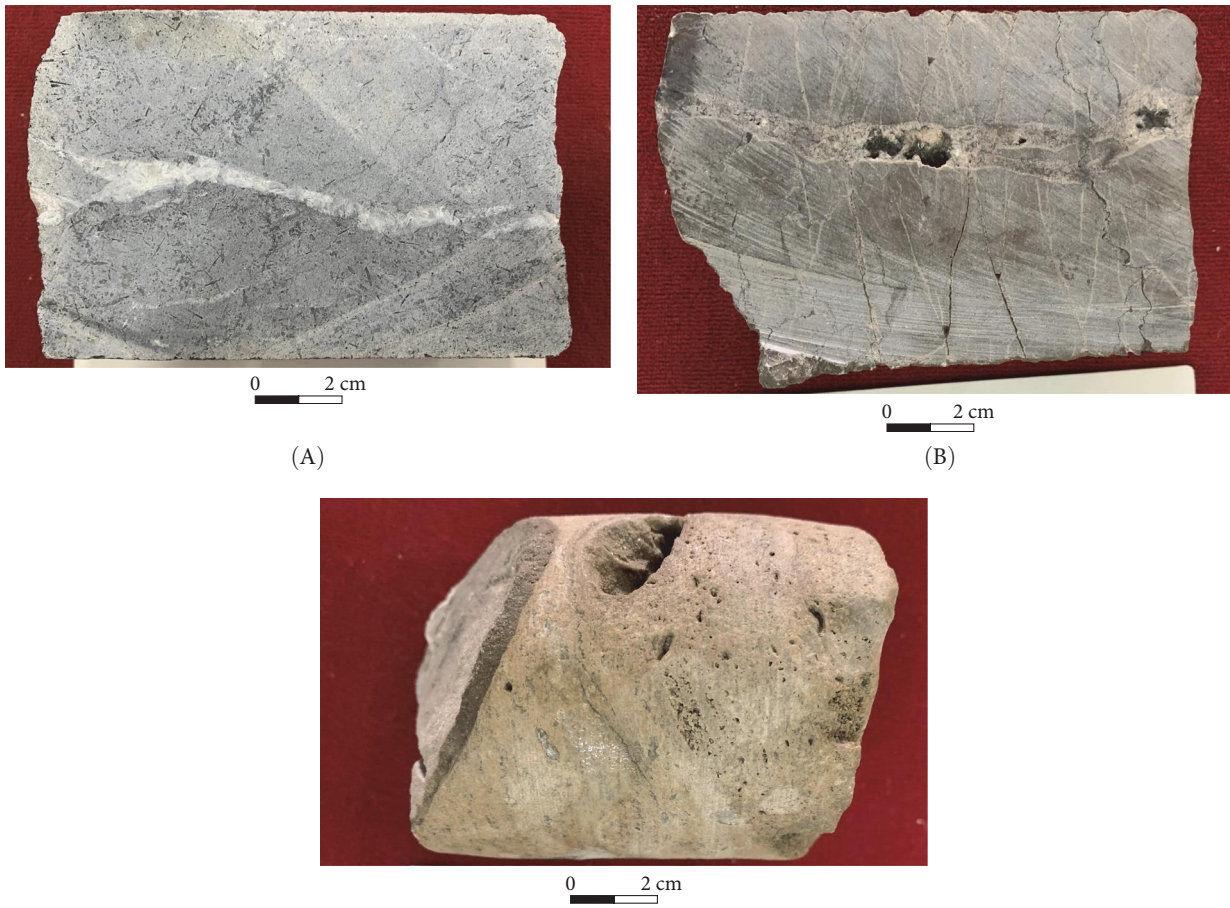

FIGURE 4: Core samples of selected Early to Middle Ordovician reservoir rocks in the studied reservoir, illustrating low-porosity and low-permeability host rocks and multi-phase, fault-related diagenesis: (A) tight bioclastic grainstone cut by fracture filled with euhedral calcite crystals; (B) tight wackestone cut by calcite-filled fractures with vugs, overprinted by stylolites and (C) crystalline dolomite with vugs infilling fracture.

TABLE 1: Summary of investigated geological heterogeneities (factors) and their low and high settings in the screening study.

Geological heterogeneity (factor)	Low setting	High setting
Fault zone width	Narrow (180 m)	Wide (600 m)
Complexity of flower structure configuration	Simple (no internal faults)	Complex (internal faults)
Continuity of fault core lithology	Continuous low-permeability fault uniform core	Alternating bands of low-permeability fault gouge and high-permeability breccia
Fault zone rock property (karstification)	No hydrothermal karstification (Table 3)	Hydrothermal karstification (Table 3)
Fault zone rock property (late cementation)	No late cementation overprint (Table 3)	Late cementation overprint (Table 3)
Fracture corridor occurrence	Absent	Present
Connectivity of fracture corridor to fault zone	Isolated from fault zone (where fracture present)	Connected to fault zone (where fracture corridor present)
Variability in host rock porosity and permeability	Homogeneous (Table 4)	Heterogeneous (Table 4)

Negative flower structures are less complex, being bounded by two major NE–SW-oriented fault segments, connected by a series of extensional faults that align with the NNE–SSW orientation of the local tectonic shortening direction [11]. These structures originated during the Middle-Late Ordovician [86, 87].

Table 2: Parameter and designing settings for the 32 constructed models in the screening study (l = low setting, h = high setting).

Heterogeneity (factor)	Model number																															
	1	2	3	4	5	6	7	8	9	10	11	12	13	14	15	16	17	18	19	20	21	22	23	24	25	26	27	28	29	30	31	32
Fault zone width	l	h	l	h	l	h	l	h	l	h	l	h	l	h	l	h	l	h	l	h	l	h	l	h	l	h	l	h	l	h	l	h
Complexity of flower structure configuration	l	l	h	h	l	l	h	h	l	l	h	h	l	l	h	h	l	l	h	h	l	l	h	h	l	l	h	h	l	l	h	h
Continuity of fault core lithology	l	l	l	l	h	h	h	h	l	l	l	l	h	h	h	h	l	l	l	l	h	h	h	h	l	l	l	l	h	h	h	h
Fault zone rock property (karstification)	l	l	l	l	l	l	l	l	h	h	h	h	h	h	h	h	l	l	l	l	l	l	l	l	h	h	h	h	h	h	h	h
Fault zone rock property (late cementation)	l	l	l	l	l	l	l	l	l	l	l	l	l	l	l	l	h	h	h	h	h	h	h	h	h	h	h	h	h	h	h	h
Fracture corridor occurrence	l	h	h	l	h	l	l	h	l	h	h	l	h	l	l	h	l	h	h	l	h	l	l	h	l	h	h	l	h	l	l	h
Connectivity of fracture corridor to fault zone	l	h	h	l	l	h	h	l	h	l	l	h	h	l	l	h	l	h	h	l	l	h	h	l	h	l	l	h	h	l	l	h
Variability in host rock porosity and permeability	h	h	l	l	l	l	h	h	l	l	h	h	h	h	l	l	l	l	h	h	h	h	l	l	h	h	l	l	l	l	h	h

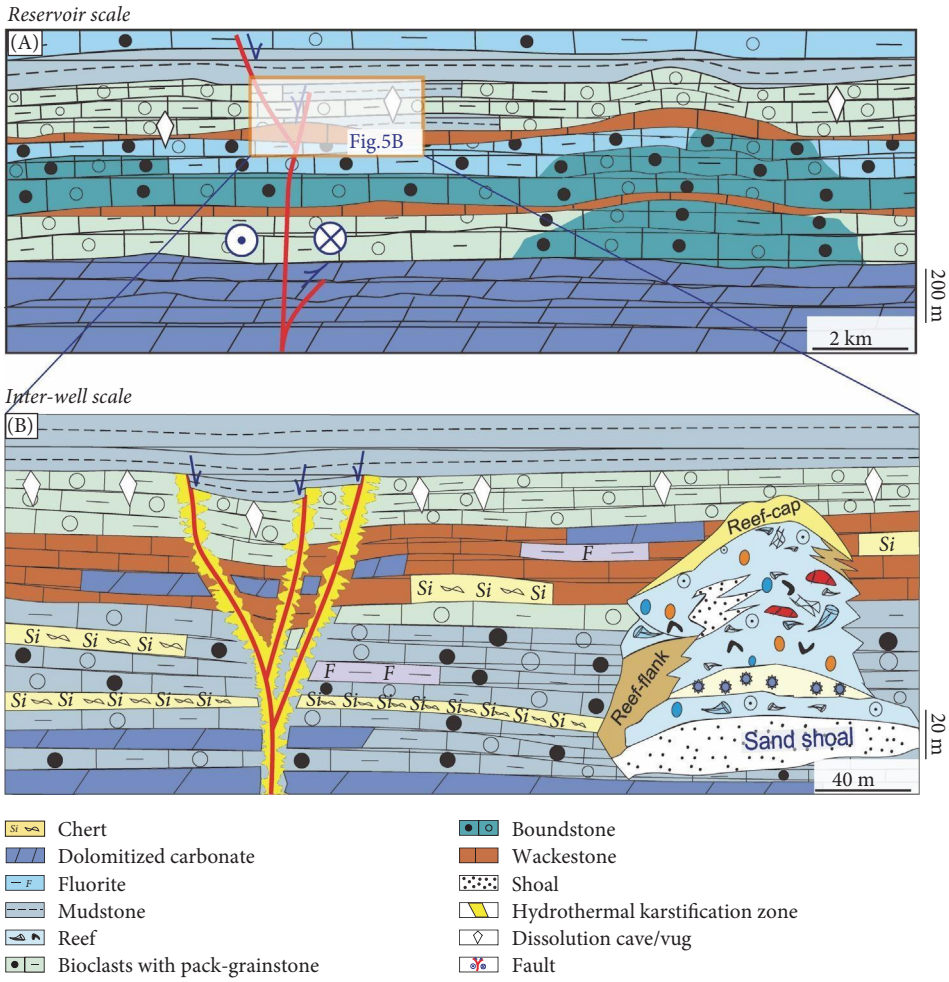

FIGURE 5: Cartoons illustrating hierarchy of geological heterogeneities across different length scales in the studied reservoir: (A) reservoir-scale architecture, consisting of laterally continuous layers of bioclastic packstone–grainstone, boundstone, wackestone and dolomitized carbonate and carbonate 'mound' containing vertically stacked reef–shoal complexes. This configuration reflects the potential matrix heterogeneity. Dissolution cavities and vugs are formed by hypogenic karstification during deep burial (modified after [51]), and (B) inter-well scale architecture, including hypogenic karstification generated by hydrothermal fluid movement and late cementation developed along faults and fractures. Reef–shoal complexes are interpreted following the seismic-attribute analysis of Dong et al. [38] and are inferred to contain relatively high porosity and permeability [12].

In order to evaluate the relative impact of these secondary faults, we constructed models that either lack (low setting) or contain them (high setting) (Table 1). In the high setting, four second-order faults are included in each flower structure. For the negative flower structures, all second-order faults strike NNE–SSW, with three of them dipping WNW and converging with another second-order fault that dips ESE. Host rock strata in the negative flower structure are offset downwards by 250 m, and an interval of overlying seal lithologies is added. Conversely, for the positive flower structure, second-order faults strike ENE-WSW, and three second-order faults dip NNW and merge with another second-order fault dipping SSE. Host rock strata in the positive flower structure are offset upwards by 350 m. Each secondary fault has a total width of 70 m, comprising a fault core of 20 m width, flanked by two fault damage zones, each 25 m wide. These second-order faults are included in small-scale models of representative volumes of negative and positive flower structures (e.g., Figure 6D), which are used to derive effective porosity and permeability values that are applied in the larger-scale models (e.g., Figure 6C).

3.2.3. Continuity of Fault Core Lithology. Fault cores may contain different lithologies separated by sharp boundaries, due to the complex interplay of mechanical and chemical processes during faulting [88, 89]. These lithologies include cataclasite and breccia, formed from the mechanical breakdown of the carbonate matrix, and very fine-grained, calcite- and clay-rich gouge resulting from the extreme comminution of the carbonate matrix [77, 90]. Mylonitic textures may also develop within carbonate fault cores subjected to intense ductile deformation [91]. Additionally, cavities between the fault core and damage zones can be filled with minerals precipitated from hydrothermal fluids circulating along the fault [80, 92]. Gouge and breccia typically dominate the fault core composition [88, 93–95].

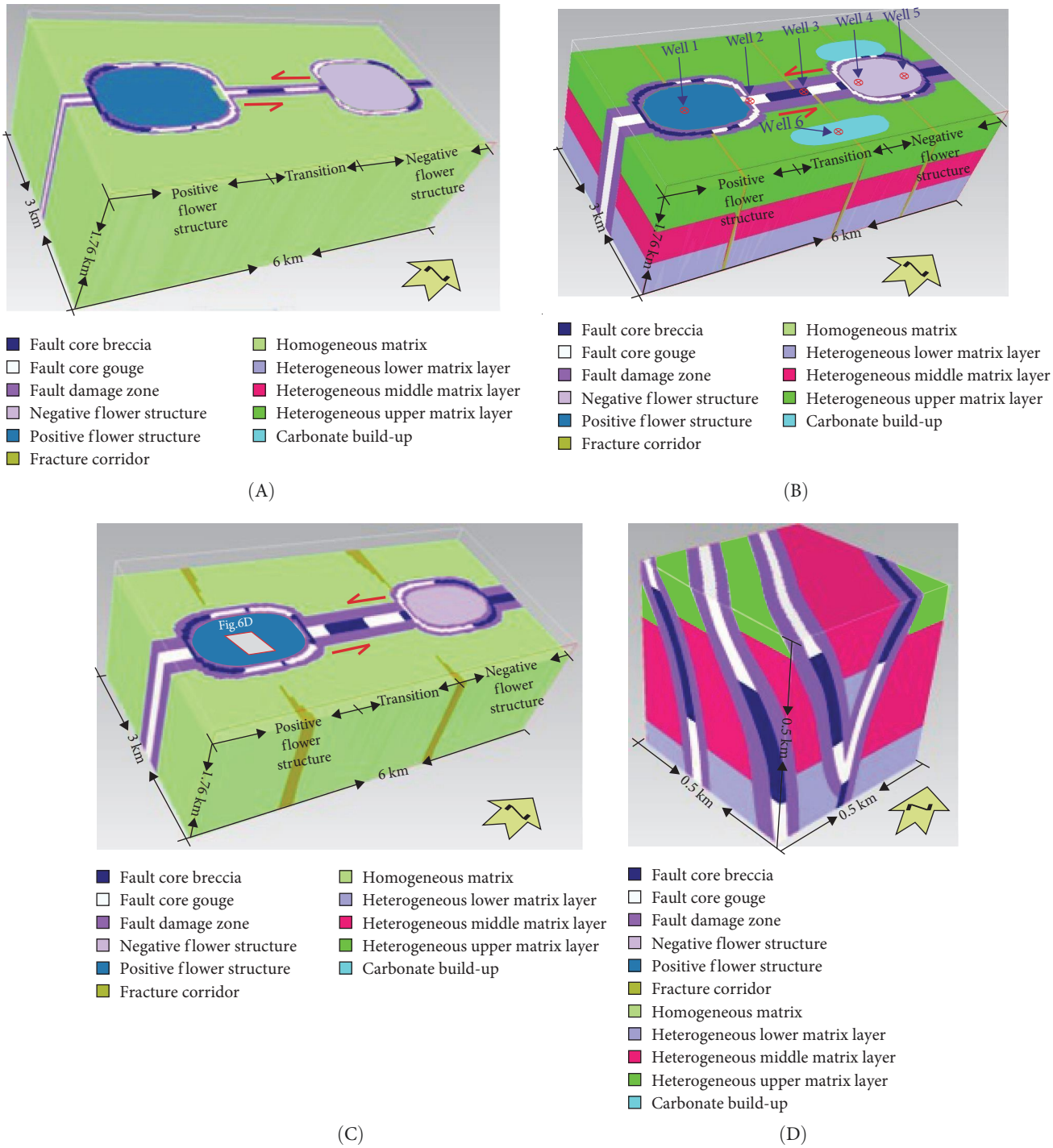

FIGURE 6: 3D perspective views of representative models: (A) model with narrow fault zone, discontinuous distribution of low-permeability fault core, no fracture corridors and homogeneous host rock; (B) model with wide fault zone, discontinuous distribution of low-permeability fault core, fracture corridors present and connected to the fault zone and heterogeneous host rock; (C) model with wide fault zone, discontinuous distribution of low-permeability fault core, fracture corridor present but not connected to the fault zone and homogeneous host rock; and (D) nested model of faults in positive flower structure, which is used to derive effective permeability values that are applied in larger-scale models (e.g., Figure 6C). Figure 6B shows the location of six wells used to calculate flow-diagnostic metrics. Components of representative model are shown in Figure 7.

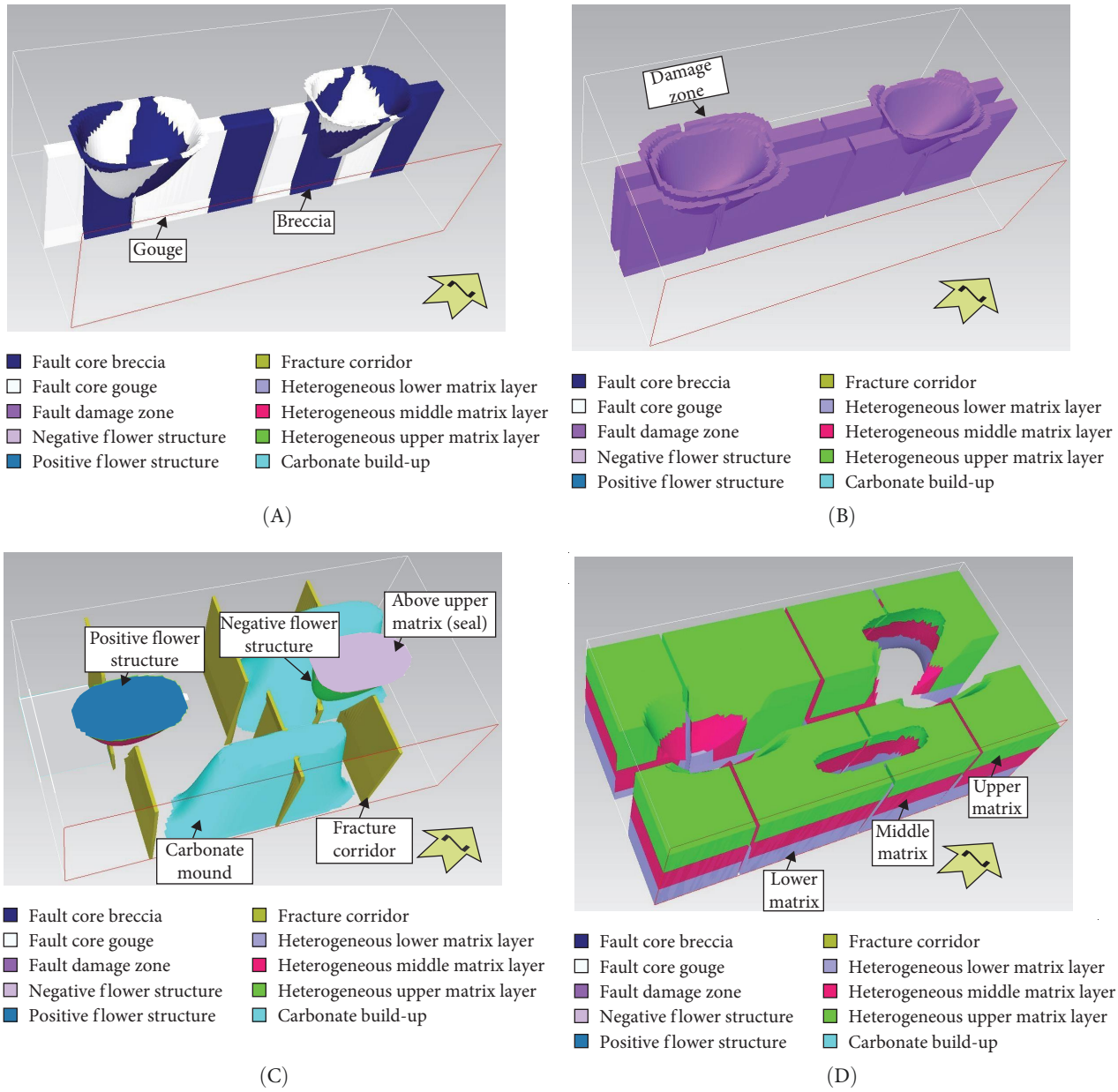

FIGURE 7: Components of representative model shown in Figure 6. (A) Fault core structure with two colors indicating fault gouge and fault breccia; (B) fault damage zone; (C) fracture corridors, carbonate mounds and flower structures associated with strike-slip fault and (D) heterogeneous host rock comprising three distinct layers in addition to carbonate mounds as shown in Figure 7C. Model dimensions are 6 km (x, parallel to fault zone strike) × 3 km (y, perpendicular to fault zone strike) × 1.76 km (z, thickness) (Figure 6A–C).

We investigated the impact of variations in fault core lithology by comparing continuous, low-permeability fault gouge (low setting) and alternating bands of low-permeability fault gouge and high-permeability breccia (high setting). In the high setting, each gouge and breccia band has a length of 650–1450 m along the fault strike (Figure 7A). Gouge and breccia regions within the flower structures are diamond-shaped, with a length of ~1500 m perpendicular to the strike of the main strike-slip fault and a maximum width of 600–1000 m (Figure 7A). These distributions of fault-core gouge and breccia are highly simplified compared to field observations and experimental results [76, 88]. However, a conceptual model that predicts the spatial distribution of fault-core gouge and breccia in a long-lived strike-slip fault system, such as the SB1 fault (Figure 3), is lacking. The simplified distributions used in our models allow heterogeneous rock property distributions to be readily incorporated in sketch-based models (Table 1), and their impact assessed.

3.2.4. Fault Zone Rock Properties. The porosity and permeability of fault zone lithologies in the deep and ultra-deep carbonate reservoirs of the north-central Tarim Basin reflect a complex diagenetic history (Figure 4B,C), which includes hypogenic karstification by hydrothermal fluids and late, post-karstification cementation [10, 12, 64, 96]. The absence (low setting) and presence (high setting) of both karstification

Table 3: Porosity and permeability values assigned to fault zone rock types in the model ensemble (Tables 1 and 2).

Fault zone rock type	No karstification, no late cementation	Karstification, no late cementation	No karstification, late cementation	Karstification, late cementation
Fault core, gouge [20, 31, 64, 97, 98]	Porosity = 10%; permeability = 2 mD	Porosity = 15%; Permeability = 20 mD	Porosity = 2%; permeability = 1 mD	Porosity = 12%; permeability = 5 mD
Fault core, breccia	Porosity = 20%; permeability = 50 mD	Porosity = 30%; permeability = 100 mD	Porosity = 10%; permeability = 20 mD	Porosity = 25%; permeability = 60 mD
Fault core, uniform [9, 90, 98]	Porosity = 15%; permeability = 20 mD	Porosity = 25%; permeability = 80 mD	Porosity = 5%; permeability = 15 mD	Porosity = 18%; permeability = 30 mD
Fault damage zone and fracture corridors [20, 56, 67, 99]	Porosity = 5%; permeability = 500 mD	Porosity = 20%; permeability = 1000 mD	Porosity = 5%; permeability = 200 mD	Porosity = 10%; permeability = 300 mD

and late cementation are considered in our analysis (Table 1), by assigning different porosity and permeability values to fault core, damage zone and fracture corridor lithologies for each combination of these two diagenetic events (Table 3). The assigned porosity and permeability values are based on published descriptions of fault zone lithologies in the deep and ultra-deep carbonate reservoirs of the north-central Tarim Basin [9, 14, 31, 56, 64, 67, 97–99] and selected global analogs [90, 100] (Table 3).

3.2.5. Fracture Corridor Occurrence. Syn-tectonic shear can generate a set of sub-parallel fracture corridors that are oriented sub-perpendicular to major strike-slip faults [101, 102]. Such fracture corridors are documented in some deep and ultra-deep carbonate reservoirs of the north-central Tarim Basin [19, 31, 103] and may act as localized conduits for fluid flow. We investigate the absence (low setting) and presence (high setting) of fault perpendicular fracture corridors in our analysis (Table 1). Where present, fracture corridors are modeled as being up to 200 m wide (x), 0.9–1.35 km in length (y) and 1.76 km high (z) (Figure 6B,C).

3.2.6. Connectivity of Fracture Corridor to Fault Zone. In models that contain fracture corridors, we also investigate the effects of their connectivity to the strike-slip fault zone (Figure 6). Fracture corridors are modeled either as wedges of 200 m maximum width that tip out before intersecting the fault zone (low setting) or as narrow (70 m wide) cuboids that intersect the fault zone (high setting) (Table 1, Figure 6B,C). In the latter configuration, fracture corridors may enhance fluid flow between the host rock and the fault zone.

3.2.7. Variability in Host Rock Porosity and Permeability. Host rocks in deep and ultra-deep carbonate reservoirs of the north-central Tarim Basin have low porosity and permeability (e.g., Figure 4A) [50, 85]. However, the host rocks comprise different carbonate rock types (Figure 5), not all of which are sampled by wells, which may vary in their porosity and permeability. We investigate the impact of such variability by considering homogenous (low setting) and heterogeneous (high setting) porosity and permeability distributions in the host rocks (Table 1). The heterogeneous distribution of host rock types subdivides the model into three laterally continuous layers and laterally discontinuous mounds (e.g., Figures 6B and 7C,D) [38, 46]. The volume-weighted arithmetic averages of porosity and permeability for the four rock types in the heterogeneous host rock (high setting) is the same as the uniform value of porosity and permeability assigned to the homogeneous host rock (low setting). Consequently, the distribution of porosity and permeability values is the key difference between the two model settings (Table 1). Porosity and permeability values for host rock types in the two settings are taken from published descriptions of deep and ultra-deep carbonate reservoirs of the north-central Tarim Basin and are summarized in Table 4.

3.3. Sketch-Based Construction of Reservoir Models. Reservoir models were constructed using an intuitive approach that leverages sketch-based interface and modeling (SBIM) methods implemented in Open Source research code (Rapid Reservoir Modeling, RRM) [22, 23]. In this sketch-based reservoir modeling approach, geological heterogeneities are represented by surfaces (e.g., stratal boundaries, fault zone and fracture corridor boundaries, diagenetic boundaries) that demarcate geological domains. The approach complements and extends traditional ways of conceptualizing and representing geological interpretations, including maps, cross sections, and block diagrams. We use the concept of fault facies to represent geological domains associated with fault zones and fracture corridors [105]. Sketch-based reservoir models are deterministic and lend themselves to investigating multiple geological scenarios [106], for example, in screening or ranking studies that precede more complex stochastic modeling of specific scenarios.

Our sketch-based models are not intended to reproduce the detail of a specific case, but instead are more generalized. For example, our models contain a generic representation of a sinistral strike-slip fault [84], rather than the details of the SB1 fault (e.g., Figure 3). The sketch-based models are constructed without reference to a predefined grid, but grids are later used for visualization (Figures 6–8) and numerical calculations [24].

Thirty-two models were constructed following the experimental design (Table 2). Heterogeneities at large length scales were sketched first and then heterogeneities at progressively smaller length scales. Five of the eight studied heterogeneities were sketched explicitly during model construction: (1) fault zone width, (2) continuity of fault core

Table 4: Porosity and permeability values assigned to host rocks in the model ensemble (Tables 1 and 2).

Host rock rock type	Heterogeneous	Homogeneous
Seal above reservoir [9, 12, 79, 104]	Porosity = 0.5%; permeability = 0.1 mD	
Upper reservoir layer [9, 12, 79, 104]	Porosity = 3.7%; permeability = 0.6 mD	
Middle reservoir layer [9, 12, 79, 104]	Porosity = 6.2%; permeability = 0.8 mD	Porosity = 5%; permeability = 0.5 mD
Lower reservoir layer [9, 12, 79, 104]	Porosity = 4.9%; permeability = 0.3 mD	
Intra-reservoir mounds [9, 12, 79, 104]	Porosity = 7.4%; permeability = 1.6 mD	

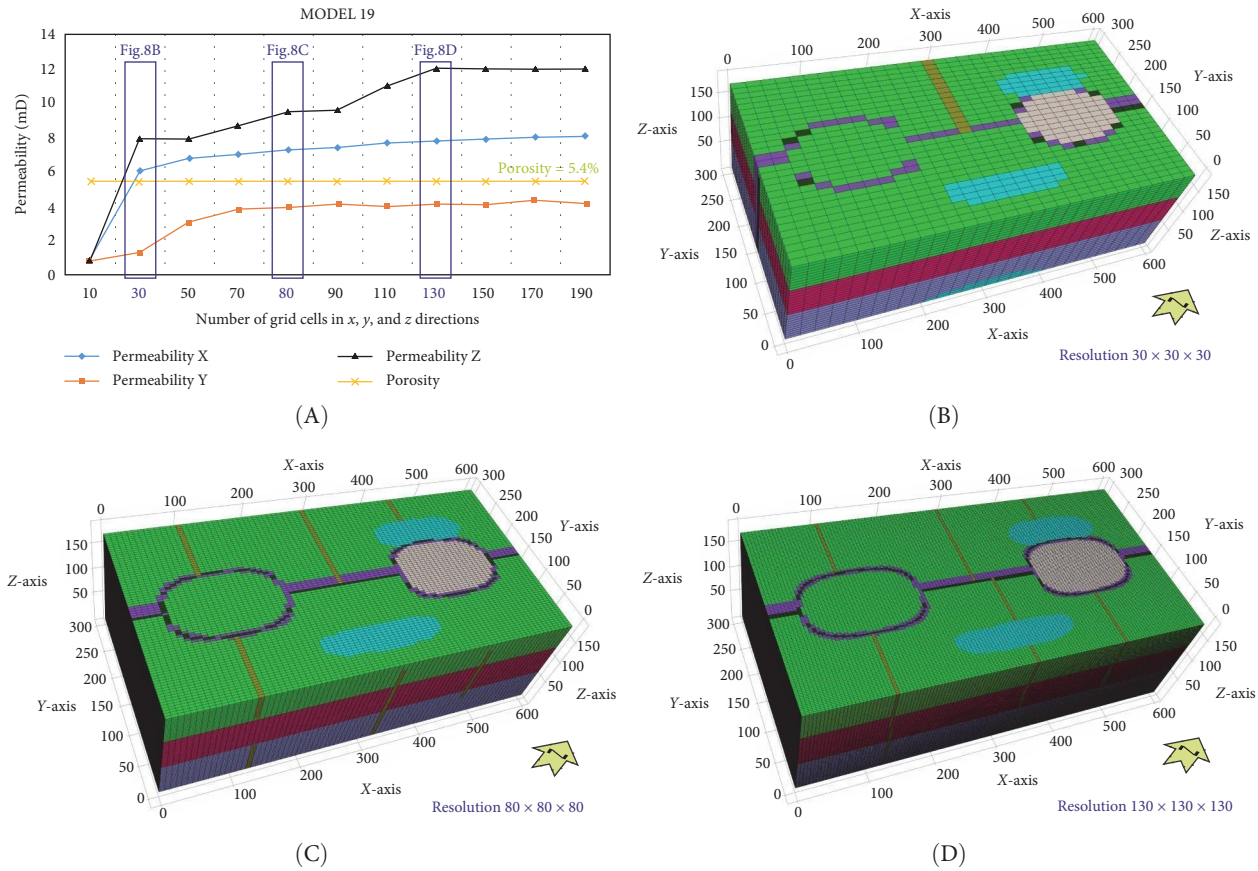

Figure 8: Sensitivity testing of grid resolution in model 19 (Table 2), which is the most geometrically complex of our ensemble of models. (A) plot of porosity and effective permeability (k_x, k_y, k_z) in model 19 for different grid resolutions. A grid resolution of 130 × 130 × 130 cells in x, y and z directions is the coarsest for which k_x, k_y and k_z are considered to be reasonably accurate. (B–D) 3D perspective views of model 19 at different grid resolutions: (B) 30 × 30 × 30 cells, (C) 80 × 80 × 80 cells and (D) 130 × 130 × 130 cells. Model dimensions are 6 km (x, parallel to fault zone strike) × 3 km (y, perpendicular to fault zone strike) × 1.76 km (z, thickness) (Figure 6A–C). Colors are the same as those used in Figures 6 and 7.

lithology, (3) fracture corridor occurrence, (4) connectivity of fracture corridors to fault zone, and (5) variability in host rock porosity and permeability (Table 1). Where combinations of the low or high settings for these heterogeneities recur in models, we reused the surfaces that define the heterogeneities in order to maintain consistency of geological-domain geometries and volumes between models. A further heterogeneity was represented in relatively small-sketched models (e.g., Figure 6D) that were used to derive effective porosity and permeability values for application in the larger sketched models (e.g., Figure 6C), (6) complexity of flower structure configuration. We constructed small sketched models of both positive and negative flower structure segments of strike-slip faults. The final two investigated heterogeneities were represented implicitly by assigning different values of porosity and permeability to geological domains,

(7) fault zone rock properties generated by karstification, and (8) fault zone rock properties generated by late cementation. The two settings of these two heterogeneities result in four combinations of porosity and permeability values that can be assigned to domains of different fault zone lithology; the values assigned to each combination were selected using published descriptions of fault rocks from the deep and ultra-deep carbonate reservoirs of the north-central Tarim Basin (Table 3).

3.4. Flow Diagnostics. Models are visually inspected to ensure that the intended structural and stratigraphic architectures are depicted accurately in the sketch-based models (e.g., Figures 6 and 7). The pore volume of the models is calculated after porosity values have been assigned to host rock types and fault zone rock types (Tables 3 and 4). Flow diagnostics enable the assessment of key flow properties and behaviors by solving a single-phase, steady-state pressure field for specific boundary conditions and fluid injection and production well combinations [107, 108]. Calculated flow properties include effective permeability, recovery rate after injection of a particular fluid volume, tracer flow paths and 'time of flight', storage efficiency and proportion of production and total flow rate for each well [108]. However, flow diagnostics do not account for effects such as fluid compressibility, transient flow (e.g., gravity segregation), multiphase fluid interaction (e.g., dissolution) and fluid–rock interactions (e.g., mineralization) [24]. Flow diagnostics serve as a preliminary assessment tool for understanding the impact of geological concepts and scenarios on flow properties, prior to more detailed full physics, multiphase simulations [23, 24]. Petrovskyy et al. [24] provide a comprehensive overview of flow diagnostics implementation in the RRM code.

Volumetric calculations in our models require generation of a grid. In addition, boundary conditions, fluid viscosity and details of the locations, perforation and bottom hole pressure of the injection and production wells are necessary for flow-diagnostic computations. To ensure numerical stability, an orthogonal grid is used for these computations. Each model comprises 2.2×10^6 grid cells, with cell dimensions of 46 m (x) x 23 m (y) x 14 m (z) (i.e., each model has $130 \times 130 \times 130$ cells). Sensitivity tests indicate that this resolution captures the geometry and continuity of geological heterogeneity, as expressed in effective permeability values in x, y and z directions (Figure 8). The models are configured with no-flow boundaries at their top and bottom surfaces, reflecting that the reservoir is overlain and underlain by sealing lithologies [10]. The lateral sides of the models are assigned pressure values of 87 MPa, giving 4 MPa pressure differential from the bottom hole pressure assigned to the production wells (83 MPa); these values mimic those derived from well data in the studied reservoir [12, 104, 109]. Fluid viscosity is set at 2.7 mPa·s, based on well test results in the studied ultra-deep reservoir [110].

Each model contains six vertical production wells that are perforated over the entire thickness of the reservoir (Figure 6B). Five of these wells are situated along the strike-slip fault zone in the centre of the model: well 1 in a positive flower structure segment, wells 2 and 3 in a vertical segment and wells 4 and 5 in a negative flower structure segment. Well 6 is located in the host rock (within a 'mound' in the case of a heterogeneous host rock; Table 1) and is considered a potential future development target (Figure 3). Consequently, tracer flows from the southern, northern, western and eastern boundaries of the model towards the simulated production wells. Well placements and perforations do not reflect any specific production plan, although production wells are located along strike-slip faults in the studied reservoir (Figure 3) [10, 31].

In assessing different models, four key metrics are utilized for volumetric and flow-diagnostic calculations: (1) total pore volume, which indicates the maximum potential for fluid storage; (2) effective permeability computed in x, y and z directions using flow-based upscaling; (3) variance in the proportion of total simulated flow rate for the six production wells, which provides a measure of spatial heterogeneity in reservoir performance and (4) recovery factor (or displacement efficiency in case of fluid injection) after 0.5, 1 and 2 pore volumes injected (PVI). The third metric allows comparison of the modeled wells with published production data in the studied reservoir [10, 31]. We use visualizations of the tracer-flow time of flight to the simulated production wells to further evaluate controls on fluid flow. Production and recovery (displacement) metrics calculated for tracer flow are systematic overestimations of the real reservoir production data because they do not account for two-phase flow effects and should therefore be viewed as indicative.

4. Results

4.1. Structural and Stratigraphic Architectures. The sketch-based models (e.g., Figures 6 and 7) are visually checked for consistency with the structural and stratigraphic architecture of the studied reservoir. Although the models contain simplified representations of the investigated heterogeneities, they reflect the occurrence, distribution and interaction of these heterogeneities. The dimensions, geometries and distributions of architectural elements that recur in multiple models (e.g., in models share many of the same settings in Table 2) are maintained in the model ensemble, thus ensuring consistency between models.

4.2. Total Pore Volume. Values of total pore volume in the ensemble of 32 models vary from 1.58×10^9 m^3 (equivalent to 5.0% average porosity in model 23; Table 3) to 2.73×10^9 m^3 (8.6% average porosity in model 10; Table 3), with a mean value of 1.95×10^9 m^3 (6.2% average porosity). Variations in total pore volume due to changes in each heterogeneity setting (Table 1) range from 0.4% to 24% (Figure 9). The largest influence on total pore volume (24%) is exerted by fault zone rock properties that reflect the presence or absence of karstification (Figure 9). The second most influential factor is fault zone rock properties that reflect late cementation, the presence of which reduces pore space by 14% on average (Figure 9) and the third most influential factor is fault zone width, with a wide fault zone increasing porosity by 12% on average (Figure 9). Other heterogeneities have less influence than the confounded effects of two-factor interactions (9%; Figure 9). Variability in the distribution of host rock porosity

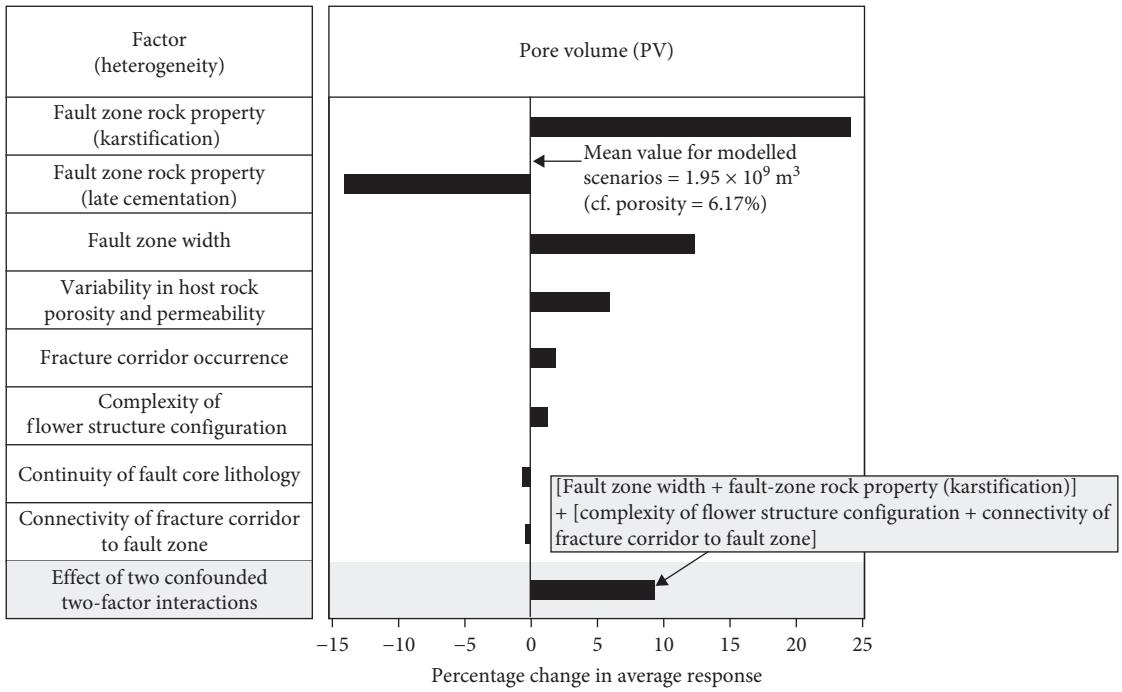

FIGURE 9: Tornado chart showing average percentage changes in total pore volume due to varying each geological heterogeneity (factor) from its low setting to its high setting (Table 1). Bars extending to the right indicate a positive change. For example, assigning properties to the fault zone that reflect karstification (high setting) increases the total pore volume by 24% compared to assigning properties that do not reflect such karstification (low setting). The chart also compares the largest responses from confounded two-factor interactions with the main effects of individual factors. Changes in total pore volume are less than 25% for all factors.

and permeability has little impact on the total pore volume (6.0% on average; Figure 9), and other heterogeneities have even less effect, each contributing less than 2% on average to the total pore volume variability (Figure 9). These results are expected, given that pore space in the models resides principally within the fault zones (Table 3) rather than the host rock (Table 4).

4.3. Effective Permeability. Values of effective permeability in the model ensemble demonstrate considerable anisotropy, with mean values of 37.5 mD in the horizontal orientation parallel to fault zone strike (k_x), 3.6 mD in the horizontal orientation perpendicular to fault zone strike (k_y) and 43.0 mD in the vertical orientation (k_z). The three heterogeneities with the largest influence on k_x are fault zone width (99% on average), fault zone rock properties that reflect late cementation (91% on average) and fault zone rock properties that reflect karstification (64% on average) (Figure 10A). Other heterogeneities have considerably less influence on average (<9%; Figure 10A) than the confounded effects of two-factor interactions (50% on average; Figure 10A).

The presence or absence of fracture corridors has the largest impact on k_y, which increases by 158% on average in models in which fracture corridors are present (Figure 10B). The connectivity of fracture corridors to the fault zone is the second most influential factor, with k_y increasing by 148% on average in models in which there is connectivity (Figure 10B). Other heterogeneities have a less significant impact than the confounded effects of two-factor interactions (148% on average; Figure 10B).

The three heterogeneities with the largest influence on k_z are, respectively, fault zone rock properties that reflect late cementation (98% on average), fault zone width (86% on average) and fault zone rock properties that reflect karstification (63% on average) (Figure 10C). The confounded effects of two-factor interactions have more impact (44% on average) than other individual heterogeneities (Figure 10C).

In directions parallel to the fault zone, effective permeability (k_x, k_z) is controlled by the width and rock properties of the fault zone, either by determining the volume of high permeability rock in the fault zone, through which fluids flow (e.g., Figure 11), or by directly governing the permeability of the fault zone rock. Conversely, in the direction perpendicular to the fault zone, effective permeability (k_y) is controlled by the presence and connectivity of fracture corridors, which act as conduits for fluid flow (e.g., Figure 12).

4.4. Variance in the Contribution of Each Well to Total Simulated Production Rate. The mean variance in the percentage contribution of each well to total simulated flow rate is 210 (i.e., standard deviation of 14.6%), which indicates a substantial variation in well performance across the ensemble of models. The three heterogeneities with the largest influence on the percentage contribution of each well to total simulated flow rate are fault zone width (44% on average), the presence or absence of fracture corridors (35% on average) and connectivity of fracture corridors to the fault zone (26% on average) (Figure 13). These three heterogeneities are among those that control effective permeability (Figure 10) and define conduits for fluid flow into some of the wells

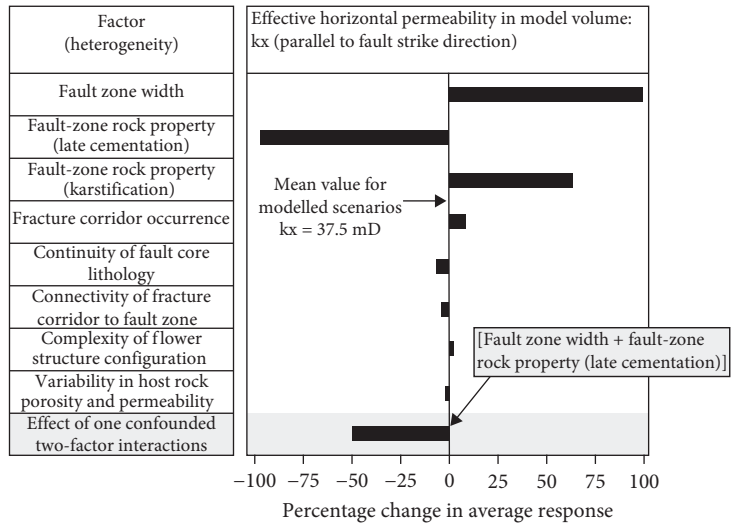

(A)

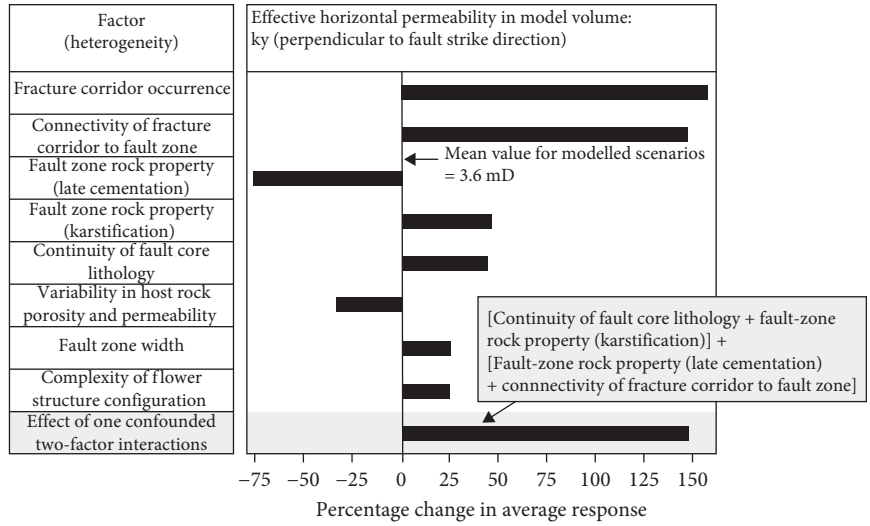

(B)

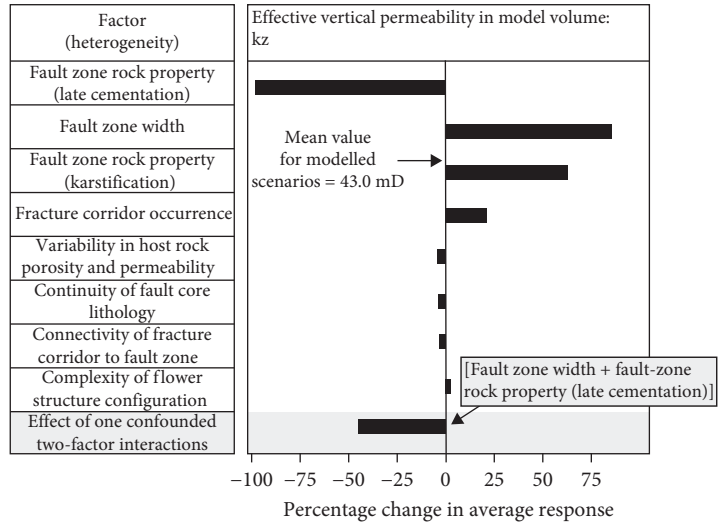

(C)

FIGURE 10: Tornado charts showing the average percentage changes in: (A) effective horizontal permeability parallel to fault zone strike (k_x); (B) effective horizontal permeability perpendicular to fault zone strike (k_y) orientations and (C) effective vertical permeability (k_z) that result from varying each factor from its low setting to its high setting (Table 1). Bars extending to the right indicate a positive change. For each chart, the largest response of confounded two-factor interactions is shown for comparison with the main effects of individual factors.

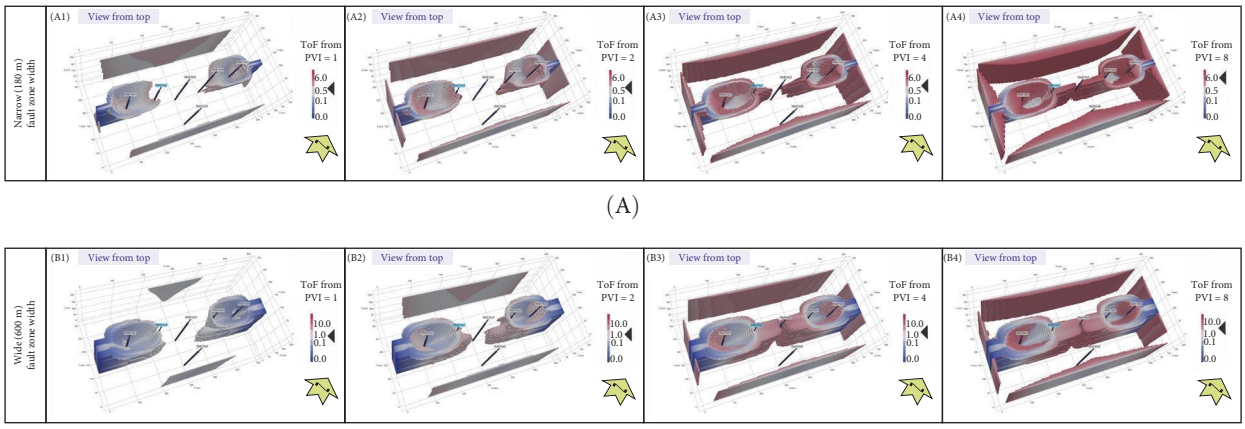

FIGURE 11: 3D perspective views of simulated tracer flow time of flight from six producing wells (Figure 6B) in selected models, highlighting the impact of fault zone width: (A) time of flight for model 9 (Table 2) is shown after 1, 2, 4 and 8 pore volumes injected (PVI), with model viewed from top; (B) time of flight for the same model, but with fault zone width modified to the high setting (Table 1), is shown at 1, 2, 4 and 8 PVI. Each panel depicts the progression of single-phase tracer into the production wells, driven by the pressure differential between the wells and the lateral model boundaries. Model dimensions are 6 km (x, parallel to fault zone strike) × 3 km (y, perpendicular to fault zone strike) × 1.76 km (z, thickness) (Figure 6A–C).

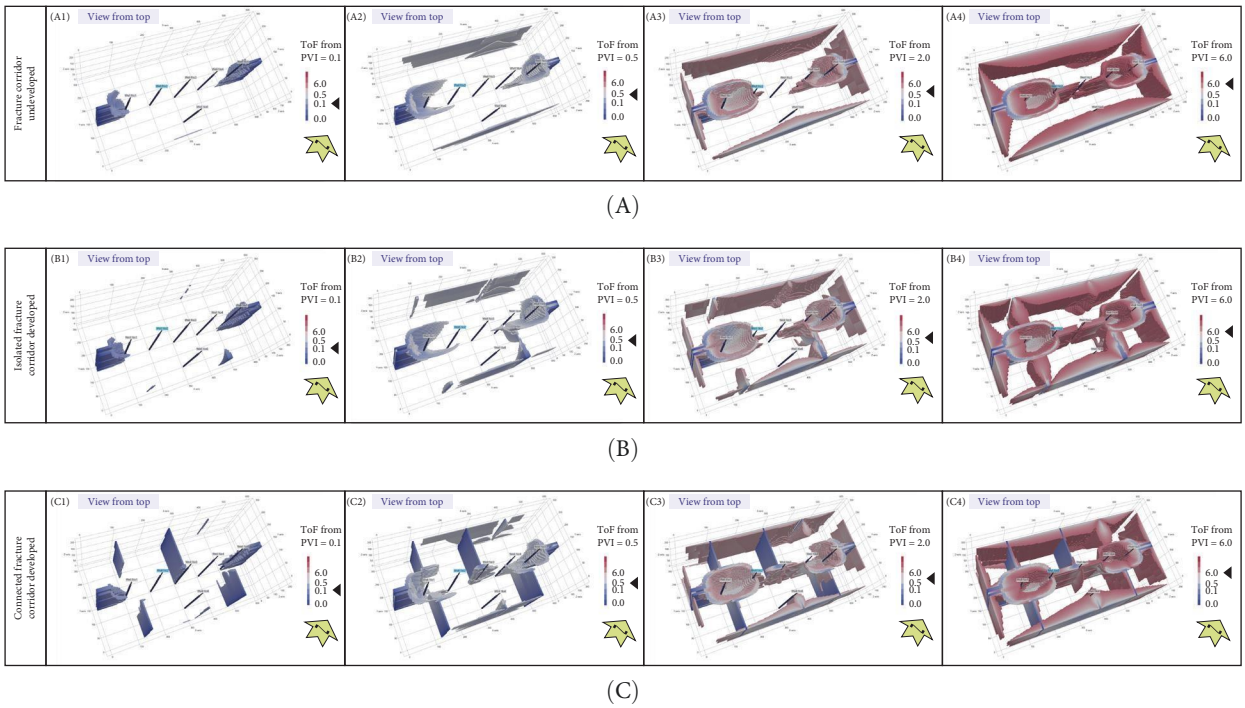

FIGURE 12: 3D perspective views of simulated tracer flow from six producing wells (Figure 6B) in selected models, highlighting the impact of fracture corridors: (A) time of flight for model 7 (Table 2), but with low setting for complexity of flower structure configuration and high setting for fault zone property (karstification, no late cementation) (Table 1), is shown at 0.1, 0.5, 2 and 6 PVI, viewed from top; this model lacks fracture corridors; (B) time of flight for the same model, but with fracture corridors isolated from the fault zone (low setting in Table 1), is shown at 0.1, 0.5, 2 and 6 PVI and (C) time of flight for the same model, but with fracture corridors connected to the fault zone (high setting in Table 1), is shown at 0.1, 0.5, 2 and 6 PVI. Each panel depicts the progression of single-phase tracer into the production wells, driven by the pressure differential between the wells and the lateral model boundaries. Model dimensions are 6 km (x, parallel to fault zone strike) × 3 km (y, perpendicular to fault zone strike) × 1.76 km (z, thickness) (Figure 6A–C).

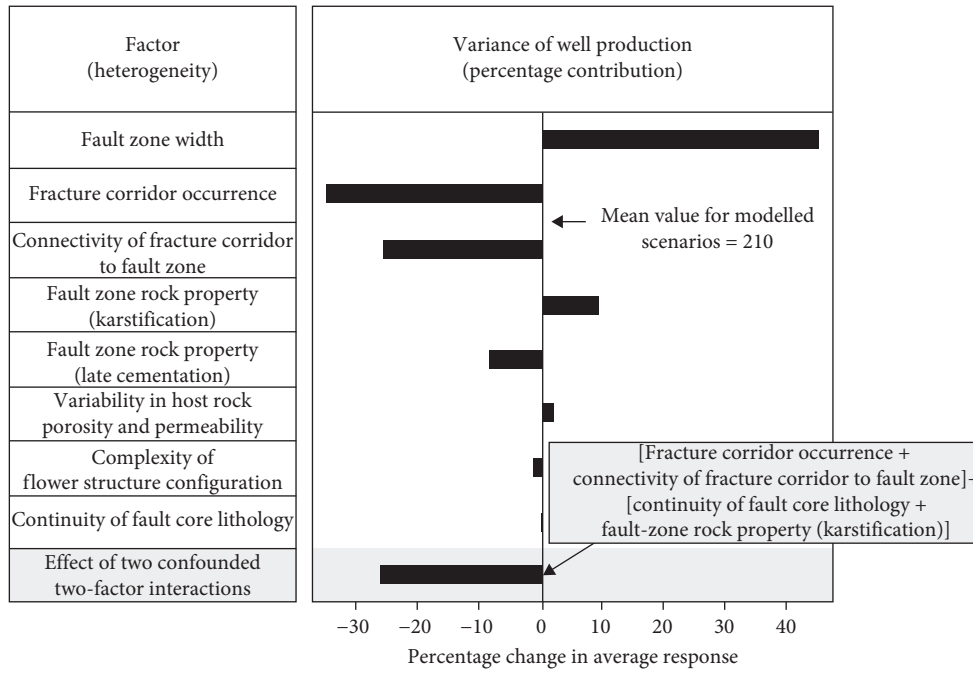

FIGURE 13: Tornado chart showing the average percentage change in the variance of the percentage contribution of each well to total simulated flow rate that results from varying each factor from its low setting to its high setting (Table 1). Bars extending to the right indicate a positive change. The largest response of confounded two-factor interactions is shown for comparison with the main effects of individual factors.

(Figures 11 and 12). Other heterogeneities have considerably less influence on average (<9%; Figure 13) than the confounded effects of two-factor interactions (26% on average; Figure 13).

4.5. Recovery Factor. The mean recovery factors at 0.5, 1 and 2 PVI for tracer flow are 20.2%, 28.9% and 40.3%, respectively. These recovery factors indicate that much of the pore volume has not been contacted (i.e., only a small fraction of the resident fluid in each model has been displaced), even after large volumes of fluid have been injected, as indicated by large volumes of produced tracer. At 0.5 and 1 PVI, the two heterogeneities with the largest influence on recovery factor are fault zone width (29% on average at 0.5 PVI, 17% on average at 1 PVI) and fault zone rock properties that reflect karstification (27% on average at 0.5 PVI, 22% on average at 1 PVI) (Figure 14). The confounded effects of two-factor interactions have more impact (13% on average at 0.5 PVI, 16% on average at 1 PVI) than other individual heterogeneities (<6% on average at 0.5 PVI, <7% on average at 1 PVI) (Figure 14). Individual heterogeneities have less impact on recovery factor at 2 PVI (and less than the confounded effects of two-factor interactions (18% on average; Figure 14). The three heterogeneities with the largest influence on recovery factor at 2 PVI are fault zone rock properties that reflect karstification (12% on average), fault zone rock properties that reflect late cementation (11% on average) and variability in host rock porosity and permeability (9% on average) (Figure 14). Thus, the impact of individual heterogeneities on recovery factor decreases as more fluid is produced, and the dominant heterogeneities also change (Figure 14). These changes occur because recovery factor is initially dominated by production of fluids from the fault zone (e.g., at 0.5 and 1 PVI; Figures 11, 12 and 14) but increasingly reflects fluids from the host rock recharging the fault zone (e.g., at 2 PVI and greater; Figures 11, 12 and 14).

5. Discussion

5.1. Controls on Fluid Storage and Production. Our results highlight that the following heterogeneities significantly influence total pore volume, effective permeability (k_x, k_y, k_z), variability in well contribution to total simulated flow rate and recovery factor within the selected settings of this study (Table 1): (1) fault zone width; (2, 3) fault zone rock properties that reflect karstification and late cementation; (4) the occurrence of fracture corridors and (5) fracture corridor connectivity to fault zones (Figures 10–14). These results are consistent with those of previous studies on the studied reservoir and other deep and ultra-deep Ordovician carbonate reservoirs in the Tarim Basin [10, 12, 31, 87, 111]. For instance, the SB3 fault, which has a relatively narrow fault zone, is associated with much lower well production than the nearby SB1 fault, which has a relatively wide fault zone, in the studied reservoir (Figures 1C and 3) [10]. Additionally, late cementation of calcite and quartz is observed to diminish reservoir performance in the central Tarim Basin [64, 66, 67, 69]. Regions of the host rock that are distant from strike-slip faults may contribute to flow via fracture corridors (Figures 10B, 12 and 13), which may help to account for anomalously high production rates in some wells (e.g., Figure 15).

Our results indicate that the complexity in structural configuration of negative and positive flower structures along strike-slip faults and the continuity of different lithologies

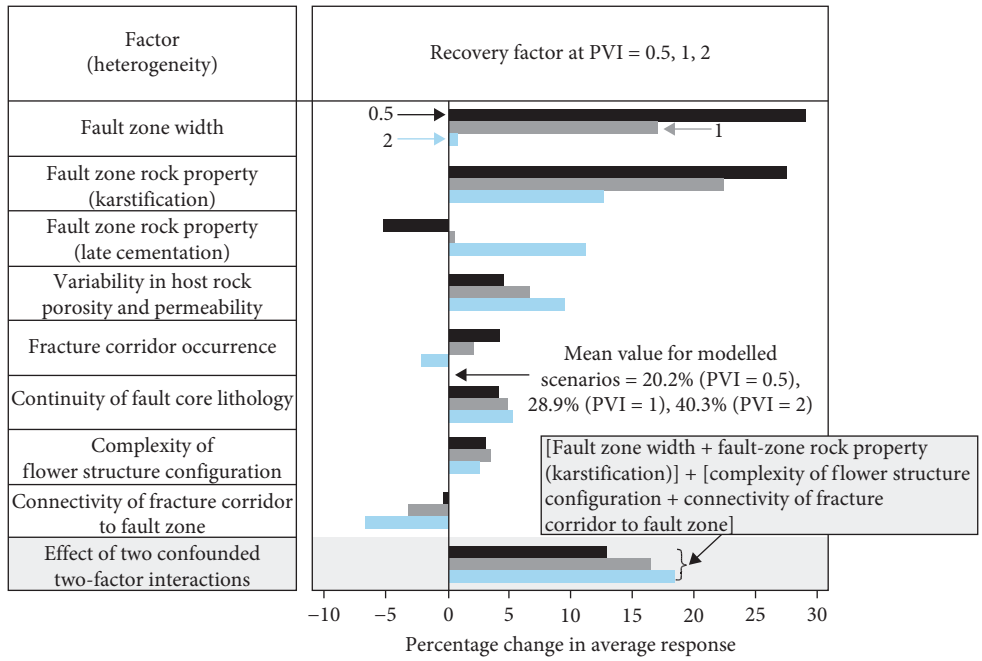

FIGURE 14: Tornado chart showing the average percentage changes in recovery factor at 0.5 (black), 1 (gray) and 2 (blue) PVI, as a result of varying each factor from its low setting to its high setting (Table 1). Bars to the right indicate a positive change. The largest response of confounded two-factor interactions is shown for comparison with the main effects of individual factors.

(gouge, breccia) in fault cores do not appear to significantly affect total pore volume, effective permeability (k_x, k_y, k_z), variability in well contribution to total simulated flow rate and recovery factor (Figures 9–14) for the settings of these heterogeneities used in this study (Table 1). However, there are important differences in the contribution of wells in negative flower structure, positive flower structure and transition segments of the strike-slip fault zone to total simulated flow rate in our models (Figure 15), with wells 2 and 3 in the transition segment and well 4, near the margins of the negative flower structure, making the largest contributions to the total simulated production rate on average (Figure 15). These results are discussed further in the following section.

Our results also indicate that variability in host rock porosity and permeability, over the range defined by the settings of this study (Table 1), has little influence on effective reservoir properties and reservoir performance (Figures 9–14). However, their influence on recovery factor increases through time, which is attributed to fluids from the host rock recharging the fault zone (e.g., at 2 PVI and greater; Figures 11, 12 and 14). Regions of the reservoir distant from the strike-slip faults have been sparsely drilled to date, and it is possible that relatively porous and permeable lithologies may occur but have not yet been sampled (e.g., in seismically imaged mounds) [38].

In summary, our results indicate that reservoir performance is strongly dependent on the permeability architecture defined by faults and fracture corridors, consistent with previous studies of fractured reservoirs with low matrix porosity and permeability [112, 113]. However, our results also highlight the interactions between fault- and fracture-related heterogeneities (e.g., Figures 11 and 12), and their relative importance for the range of heterogeneity properties considered for the studied ultra-deep carbonate reservoirs (e.g., Figures 9 and 10). These results were generated rapidly and efficiently and encompass uncertainty in geological interpretation, thus emphasizing the value of our screening methodology.

Finally, it is important to recognize that the regional and local *in situ* stress field, detailed history of burial-related structural diagenesis and mechanical evolution of the fault zone rocks during production are not considered in our models and screening study. Either individually or in combination, these additional heterogeneities could play a major role in reservoir quality, compartmentalization and production behavior [54, 111]. Using borehole image logs from wells neighboring the study area, Zhao et al. [111] interpreted critically stressed fractures to have sub-vertical dips and to strike NNE-SSW to NE–SW, sub-parallel to the SB1 and SB3 faults (Figure 3). Their analysis indicates that fractures with these orientations are likely to be dilatant and open to flow. By inference, fracture corridors perpendicular to the major strike-slip faults, and also normal and reverse faults within negative and positive flower structures, may be closed under the regional *in situ* stress field; this interpretation is comparable to assigning low settings for fracture corridor occurrence and complexity of flower structure configuration in our models (Table 1).

5.2. Comparison to Production Data. Well production data from the studied reservoir indicate that it is at least partly compartmentalized between negative flower structure, positive flower structure and transitional segments of the SB1 strike-slip fault zone [114]. Negative flower structures are characterized by high oil storage, high pressure and high

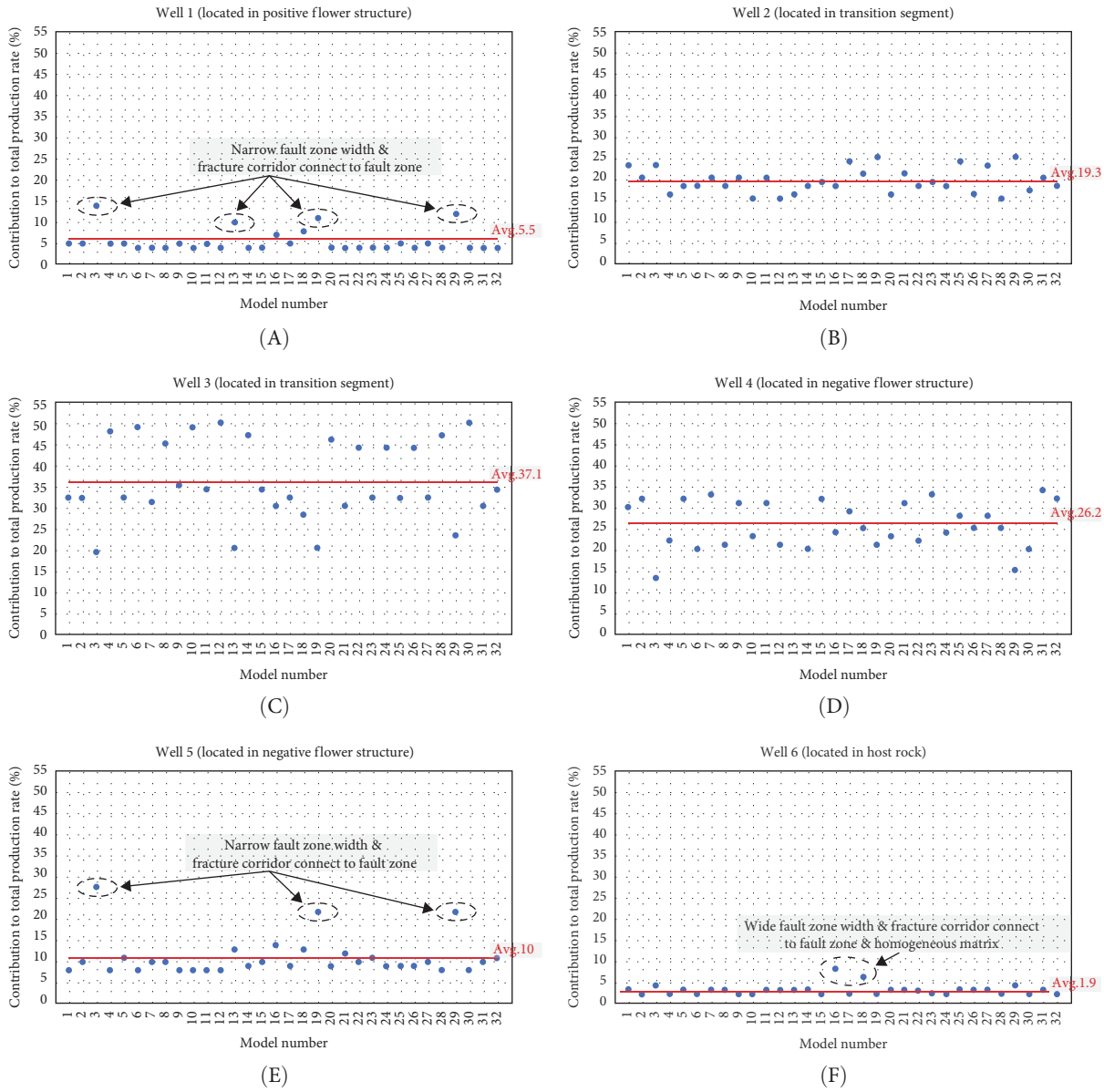

FIGURE 15: Plots showing the percentage contribution of each well to total simulated flow rate in the 32 models used in this study (Table 2): (A) well 1, located in a positive flower structure segment of the strike-slip fault zone (Figure 6B); (B) well 2 and (C) well 3, which are both located in a transition segment of the strike-slip fault zone (Figure 6B); (D) well 4 and (E) well 5, which are both located in a negative flower structure segment of the strike-slip fault zone (Figure 6B); and (F) well 6, which is located in the host rock (Figure 6B). The average performance of each well is shown and compared with published production data for the studied reservoir in Figure 15.

single-well productivity [10, 31]. Production curves for wells along such fault zones typically exhibit an initial rise, followed by a phase of stabilization, and subsequently diverge into either a rapid or a gradual decline phase [115].

Production wells in the studied reservoir occur with similar spacing and in similar strike-slip fault zone segments (Figure 3) as most of the wells in our models (Figures 6B, 11 and 12). Wells Z1-5, Z1-6, Z1-7, Z1-8, Z1-9 [10] and wells SB104, SB105, SB106, SB107, SB108 [31] correspond to wells 1, 2, 3, 4, and 5 in our models. Qi [10] documents daily well production rate, whereas Deng et al. [31] document production per unit pressure drop in wells. These published reservoir production data allow us to calculate the mean production rate of wells located in different types of strike-slip fault zone segment, which can then be compared to the percentage contribution of each well to total production rate in our model simulations (Figure 15).

In our model simulations, wells 2 and 3, located in the transition segment (Figure 6B), and wells 4 and 5, located in the negative flower structure (Figure 6B), are moderately to highly productive, each contributing on average 10%–37% of the total production rate (Figure 15). In contrast, wells 1 and 6, which are located in the positive flower structure and host rock (Figure 6B), contribute on average only 6% and 2%, respectively (Figure 15). Well 1 in models 3, 13, 19, and

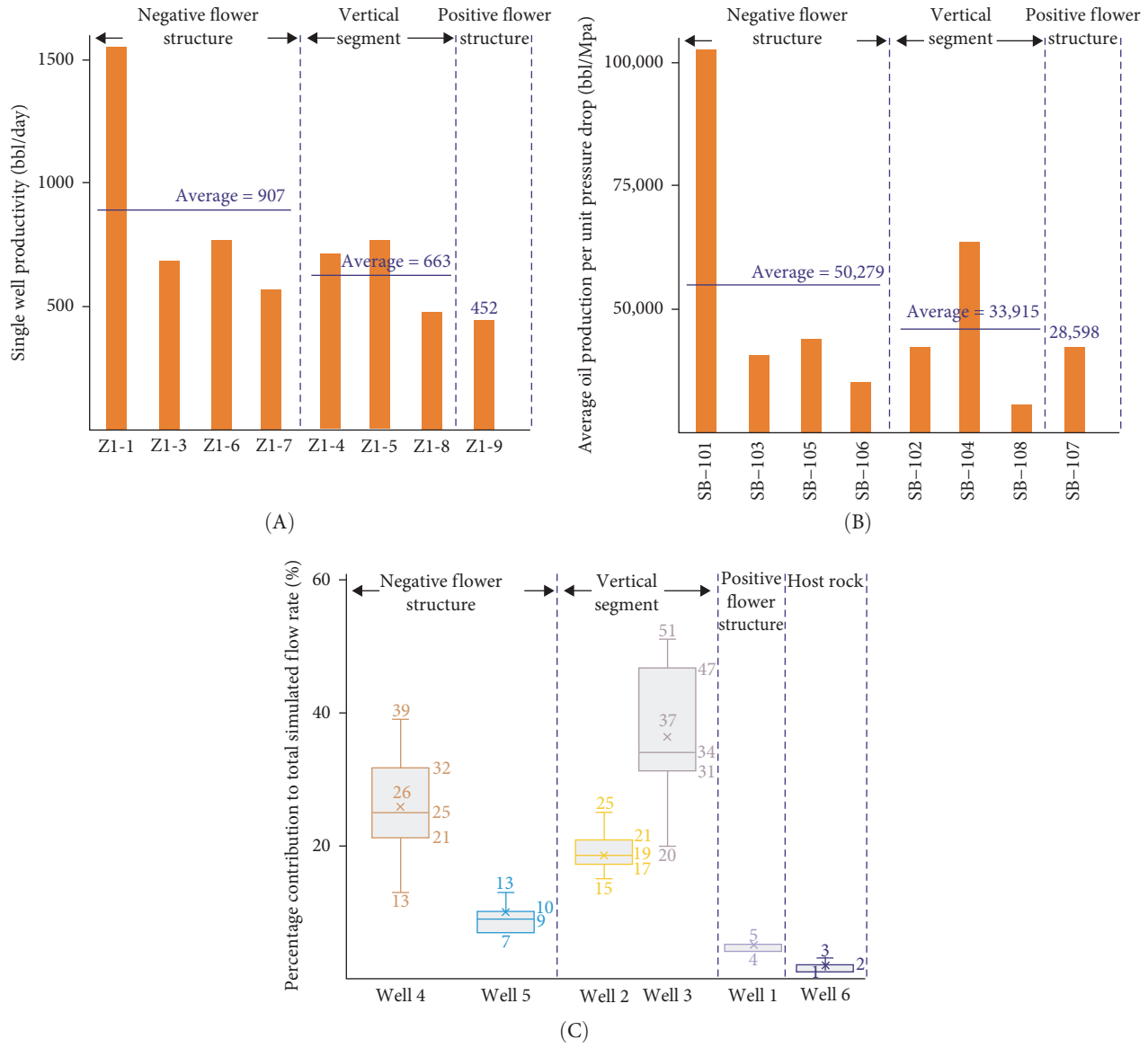

FIGURE 16: Plot comparing well performance between the production data from the studied reservoir and our flow-diagnostic simulations: (A) single well daily production rate, studied reservoir wells (after [10]); (B) single well average oil production per unit pressure drop, studied reservoir wells (after [31]) and (C) percentage contribution to total simulated flow rate of wells in the 32 models constructed for this study (Figure 6B and 15). In Figure 16C, each well is represented by a box-and-whisker: the ends of the whickers show minimum (Q0) and maximum (Q100) values, the box demarcates Q25 and Q75 values, the horizontal line in each box shows the median (Q50) value and the cross represents the mean value.

29, and well 5 in models 3, 19, and 29, show a relatively high percentage contribution to total production (Figure 15). These models are characterized by a narrow fault zone that is connected to fracture corridors (Table 1), and the relatively high contribution to production of wells 1 and 5 likely reflect flow preferentially into these wells from the nearby model boundaries along the fault zone strike and fracture corridors (Figure 12C). The anomalously high percentage contribution from well 6 in models 16 and 18 (Figure 15) is attributed to flow preferentially into this well via a fracture corridor that extends from the nearby model boundary (Figure 12C).

Wells Z1-4, Z1-5 and Z1-8 [10] and wells SB102, SB104 and S108 [31], located in the transition segments of the SB1 fault (Figure 3), contribute an average of 663 bbl of daily oil production [10] and an average 3.4×10^4 bbl oil production per MPa pressure drop [31]; in comparison, wells 2 and 3 in our models contribute an average of 19% and 37% to the total simulated production rate, respectively (Figure 16). Wells Z1-1, Z1-3, Z1-6 and Z1-7 [10] and wells SB101, SB103, SB105 and S106 [31] are located in a negative flower structure of the SB1 fault (Figure 3), contributing an average of 907 bbl of daily oil production [10] and an average of 5.0×10^4 bbl of oil production per MPa pressure drop [31] in comparison, wells 4 and 5 in our models contribute an average of 26% and 10% to the total simulated production rate, respectively (Figure 16). Finally, well Z1-9 [10] and well

SB107 [31], located in a positive flower structure of the SB1 fault (Figure 3), contribute 452 bbl of daily oil production [10] and 2.9×10^4 bbl of oil production per MPa pressure drop [31]; in comparison, well 1 in our models contributes an average of 5% to the total simulated production rate (Figure 16). Both field production data (Figure 16A,B) and simulated results (Figure 16C) reveal that well performance in the negative flower structure is higher than that in the positive flower structure but comparable to the transition segment. The variability in contribution to production of wells in negative flower structure, transitional and positive flower structure segments is also similar between the field production data and model flow-diagnostic simulation results (Figure 16). However, well SB101/Z1-1 shows exceptionally high production performance, three to four times higher than other wells, and occurs in an elongated negative flower structure (Figure 3) [10, 61]. No single well in our flow-diagnostic simulation results mirrors this performance (Figure 15), suggesting the need for more detailed simulation studies to follow up on the screening results presented here. Specifically, it would be beneficial to investigate scenarios characterized by heterogeneities conducive to high effective permeability values (k_x, k_y, k_z), including a combination of high fault zone width, low complexity of flower structures, continuous high-permeability rocks within the fault core, fault zone rocks that have undergone karstification without subsequent late cementation and fracture corridors connected to the fault zone (cf., Figure 10). Overall, detailed conceptual understanding and reservoir models at the scale of fault zone segments and individual wells are required to investigate the integrated effects of structural diagenesis, local stress field and geomechanical response to production [54, 111], in order to predict locations of high productivity within negative flower structure (and other) segments. Full physics, multiphase flow simulations should be conducted on these reservoir models in order to compare the results to production data directly.

5.3. Application to Low-Carbon Energy and Groundwater Resources. Similar geological heterogeneities and architectures to those investigated in the studied reservoir are documented in many groundwater aquifers, geothermal reservoirs and potential CO_2 and H_2 storage units [1–4, 7]. These heterogeneities will determine patterns of fluid flow, fluid storage and/or efficiency of resource utilization, although the detail of any specific application will depend on fluid type(s), rock–fluid interactions and additional rock properties (e.g., thermal conductivity). Most, if not all, of these low-carbon applications are in data-poor environments, which gives rise to major uncertainties. It is well-known that geological uncertainties are exacerbated in data-poor environments by human biases when interpreting data and developing geological concepts [116–119]. In these cases, scenario-based reservoir modeling should be used to avoid anchoring and provide more reliable uncertainty bounds [106]. Sketch-based reservoir modeling, as demonstrated here, is therefore, a key tool to capture the geometrical configuration of heterogeneities in prototype models of complex carbonate rocks. The workflow allows us to quickly create an ensemble of geologically plausible reservoir model scenarios and compare and contrast how different geological uncertainties and interpretations of the available data impact flow and storage processes relevant to low-carbon energy and groundwater resources. We note that the studied ultra-deep reservoir is characterized by extreme permeability variations, of up to four orders of magnitude, between low-permeability host rocks (generally <1 mD; Table 4) and high-permeability, fault zone rocks (up to 1000 mD; Table 3). This wide range of rock-property values also lies within the capabilities of flow diagnostics that are integrated in the sketch-based modeling tool [24]. The close correspondence between production data and flow-diagnostic metrics for the studied reservoir (Figure 15) further illustrates the predictive value of sketch-based modeling and flow diagnostics, particularly with complementary experimental design methods that identify where more detailed modeling and flow simulation effort should be focussed [29, 30]. In combination, our results build further confidence in the transfer of sketch-based modeling technology and knowledge from hydrocarbon applications to low-carbon resource and groundwater flow applications.

6. Conclusions

This study uses an innovative and efficient screening method that integrates experimental design, sketch-based reservoir modeling and flow diagnostics to investigate the effects of sedimentary and structural heterogeneities on the performance of ultra-deep (>7 km) carbonate reservoirs developed along major strike-slip faults in the north-central Tarim Basin, northwest China. Thirty-two models are constructed, following a two-level fractional-factorial design (2_{IV}^{8-3}). Each model contains a central strike-slip fault zone with a negative flower structure, positive flower structure and intervening vertical transition segment. Models are 6 km long (parallel to fault strike), 3 km wide (perpendicular to fault strike) and 1.76 km thick. Four metrics are used for volumetric and flow-diagnostic analysis to assess the impact of the eight studied heterogeneities: (1) total pore volume; (2) effective vertical and horizontal permeability, both along and perpendicular to fault zone strike; (3) variance in the proportion of the total simulated flow rate in six production wells located in the fault zone and host rock and (4) recovery factor after 0.5, 1 and 2 PVI.

Fault zone width has the most significant impact on reservoir performance, with wider fault zones leading to increased porosity, increased effective horizontal permeability along fault zone strike and increased variability in well performance. The presence of fracture corridors that are connected to the fault zone increases effective permeability perpendicular to fault zone strike and increases variability in well performance. Fault zone rock properties reflecting karstification and late cementation exert significant positive and negative impacts, respectively, on effective permeability in all directions. These results support the previously interpreted importance of strike-slip fault zones and fracture corridors in acting as conduits for fluid flow in the ultra-deep carbonate reservoirs. The structural complexity within flower structures

has only minor influence on effective permeability, but simulated wells in negative flower structure and transition segments of the strike-slip fault zone are more productive on average than simulated wells in positive flower structure segments, consistent with published production data from the ultra-deep reservoirs. Variation in host–rock properties and continuity of fault core lithology exert little effect on the four flow-diagnostic metrics, although both cause recovery factor to increase with the volume of fluid produced, consistent with recharge of the fault zone and fracture corridors with fluid from the host rock. Overall, the results of our screening study serve to focus future modeling and flow-simulation effort on geological heterogeneities that exert the most influence on reservoir performance. The screening method, modeling technology and specific results of this study are also directly applicable to characterization and efficient use of groundwater, geothermal and CO_2- and H_2-storage resources where data are sparse, which not only increases geological uncertainty but also expands the number of plausible geological interpretations of the available data.

Data Availability Statement

Rapid Reservoir Modeling prototype (executable and source code) is available at https://bitbucket.org/rapidreservoirmodelling/rrm. The 32 models constructed in this study are available at https://doi.org/10.6084/m9.figshare.22785533.v5.

Conflicts of Interest

The authors declare no conflicts of interest.

Funding

We are grateful to Sinopec as sponsors of the Resource Geophysics Academy at Imperial College London for supporting this research and approving this article for publication.

Acknowledgments

We acknowledge the constructively critical comments of two anonymous reviewers, and the editorial handling of Sun Mengdi and Kanaga Durga Krishnan. We are grateful to Sinopec as sponsors of the Resource Geophysics Academy at Imperial College London for supporting this research. We thank the members of Phase 1 of the Rapid Reservoir Modeling Consortium (Equinor, ExxonMobil Upstream Research Company, Petrobras, Shell and IBM Research Brazil/IBM Centre for Advanced Studies (CAS) Alberta, Canada) and Phase 2 of the Rapid Reservoir Modeling Consortium (Equinor, ExxonMobil Upstream Research Company, Petrobras, Petronas and Shell) for supporting its development and Open Source release. We also thank Dr. Cheng Huang and Dr. Bo Lin from Sinopec NW company, and Dr. Joyce Neilson and Dr. Rebecca Bell for valuable discussion and constructive suggestions on this work.

References

[1] W. B. White, "Conceptual Models for Carbonate Aquifers," *Groundwater* 7 (1969): 15–21.

[2] D. Montanari, A. Minissale, M. Doveri, et al., "Geothermal Resources Within Carbonate Reservoirs in Western Sicily (Italy): A Review," *Earth-Science Reviews* 169 (2017): 180–201.

[3] T. Burchette, "Carbonate Rocks and Petroleum Reservoirs: A Geological Perspective From Industry," in *Geological Society of London*, vol. 370 of *Advances in Carbonate Exploration and Reservoir Analysis*, (Special Publication, 2012): 17–37.

[4] G. Yang, Y. Li, A. Atrens, et al., "Reactive Transport Modeling of Long-Term CO_2 Sequestration Mechanisms at the Shenhua CCS Demonstration Project, China," *Journal of Earth Science* 28 (2017): 457–472.

[5] A. C. Bulnes and R. U. Fitting, "An Introductory Discussion of the Reservoir Performance of Limestone Formations," *Transactions of the AIME* 160 (1945): 179–201.

[6] S. M. Agar and S. Geiger, "Fundamental Controls on Fluid Flow in Carbonates: Current Workflows to Emerging Technologies," in *Geological Society of London*, 406, (Special Publication, 2015): 1–59.

[7] T. Hörbrand, K. Beichel, D. Bendias, A. Savvatis, and T. Kohl, "Karst Control on Reservoir Performance of A Developed Carbonate Geothermal Reservoir in Munich, Germany," 548 (2025).

[8] Z. Wang, Z. Gao, T. Fan, Y. Shang, L. Qi, and L. Yun, "Structural Characterization and Hydrocarbon Prediction for the SB5M Strike-Slip Fault Zone in the Shuntuo Low Uplift, Tarim Basin," *Marine and Petroleum Geology* 117 (2020): 104418.

[9] G. Wu, K. Zhao, H. Qu, et al., "Permeability Distribution and Scaling in Multi-Stages Carbonate Damage Zones: Insight From Strike-Slip Fault Zones in the Tarim Basin, NW China," *Marine and Petroleum Geology* 114 (2020): 104208.

[10] L. Qi, "Structural Characteristics and Storage Control Function of the Shun I Fault Zone in the Shunbei Region, Tarim Basin," *Journal of Petroleum Science and Engineering* 203 (2021): 108653.

[11] C. Huang, L. Yun, Z. Cao, et al., "Division and Formation Mechanism of Fault-Controlled Fracture-Vug System of the Middle-to-Lower Ordovician, Shunbei Area, Tarim Basin," *Oil & Gas Geology* 43 (2022): 54–68.

[12] Y. Ma, X. Cai, L. Yun, et al., "Practice and Theoretical and Technical Progress in Exploration and Development of Shunbei Ultra-Deep Carbonate Oil and Gas Field, Tarim Basin, NW China," *Petroleum Exploration and Development* 49, no. 1 (2022): 1–20.

[13] G. Wu, H. Yang, H. Li, and L. Sun, "Controlling Effects of the Ordovician Carbonate Pore Structure on Hydrocarbon Reservoirs in the Tarim Basin, China," *Petroleum Science* 10, no. 3 (2013): 282–291.

[14] L. Yang, L. Yu, D. Chen, K. Liu, P. Yang, and X. Li, "Effects of Dolomitization on Porosity During Various Sedimentation-Diagenesis Processes in Carbonate Reservoirs," *Minerals* 10, no. 6 (2020): 574.

[15] L. Chen, Z. Jiang, C. Sun, et al., "An Overview of the Differential Carbonate Reservoir Characteristic and Exploitation Challenge in the Tarim Basin (NW China)," *Energies* 16, no. 15 (2023): 5586.

[16] T. Duan, W. Zhang, X. Lu, M. Li, H. Zhao, and X. Shang, "Architectural Characterization of Ordovician Fault-Controlled Paleokarst Carbonate Reservoirs, Tahe Oilfield, China," *Interpretation-a Journal of Bible and Theology* 8, no. 4 (2020): T953–T965.

[17] R. Wang, J. Yang, L. Chang, et al., "3D Modeling of Fracture-Cave Reservoir From a Strike-Slip Fault-Controlled Carbonate

Oilfield in Northwestern China," *Energies* 15, no. 17 (2022): 6415.

[18] W. Zhang, Z. He, T. Duan, Q. Ma, M. Li, and H. Zhao, "Architecture Characteristics and Characterization Methods of Fault-Controlled Karst Reservoirs: A Case Study of the Shunbei 5 Fault Zone in the Tarim Basin, China," *Interpretation—A Journal of Bible and Theology* 11, no. 1 (2023): SA47–SA62.

[19] J. N. Méndez, Q. Jin, M. González, et al., "Fracture Characterization and Modeling of Karsted Carbonate Reservoirs: A Case Study in Tahe Oilfield, Tarim Basin (Western China)," *Marine and Petroleum Geology* 112 (2020): 104104.

[20] W. B. Zhang, Y. X. Zhang, T. Z. Duan, M. Li, H. W. Zhao, and Y. Wang, "Hierarchy Modeling of the Ordovician Fault-Karst Carbonate Reservoir in Tuoputai Area, Tahe Oilfield, Tarim Basin, NW China," *Oil & Gas Geology* 43 (2022): 207–218.

[21] T. Duan, W. Zhang, Z. He, et al., "Deep Learning-Based Geological Modeling of Ultra-Deep Fault-Karst Reservoirs in Shunbei Oilfield, Tarim Basin," *Oil & Gas Geology* 44 (2023): 203–212.

[22] M. Costa Sousa, J. D. M. Silva, C. C. M. M. Silva, et al., "Smart Modelling of Geologic Stratigraphy Concepts Using Sketches," in *Smart Tools and Apps for Graphics—Eurographics Italian Chapter Conference*, (The Eurographics Association, 2020): 89–100.

[23] C. Jacquemyn, M. E. Pataki, G. J. Hampson, et al., "Sketch-Based Interface and Modelling of Stratigraphy and Structure in Three Dimensions," *Journal of the Geological Society of London* 178 (2021): 2020–2187.

[24] D. Petrovskyy, C. Jacquemyn, S. Geiger, et al., "Rapid Flow Diagnostics for Prototyping of Reservoir Concepts and Models for Subsurface CO_2 Storage," *International Journal of Greenhouse Gas Control* 120 (2023): 103855.

[25] M. Fadel, J. Reinecker, D. Bruss, and I. Moeck, "Causes of a Premature Thermal Breakthrough of a Hydrothermal Project in Germany," *Geothermics* 105 (2022): 102523.

[26] M. Fadel, E. M. Rioseco, P. O. Bruna, and I. Moeck, "Pressure Transient Analysis to Investigate a Coupled Fracture Corridor and a Fault Damage Zone Causing an Early Thermal Breakthrough in the North Alpine Foreland Basin," *Geoenergy Science and Engineering* 229 (2023): 212072.

[27] A. Daniilidis, S. Saeid, and N. G. Doonechaly, "The Fault Plane as the Main Fluid Pathway: Geothermal Field Development Options under Subsurface and Operational Uncertainty," *Renewable Energy* 171 (2021): 927–946.

[28] R. E. Rizzo, N. F. Inskip, H. Fazeli, et al., "Modelling Geological CO_2 Leakage: Integrating Fracture Permeability and Fault Zone Outcrop Analysis," *International Journal of Greenhouse Gas Control* 133 (2024): 104105.

[29] W. A. Jackson, G. J. Hampson, C. Jacquemyn, et al., "A Screening Assessment of the Impact of Sedimentological Heterogeneity on CO_2 Migration and Stratigraphic-Baffling Potential: Johansen and Cook Formations, Northern Lights Project, Offshore Norway," *International Journal of Greenhouse Gas Control* 120 (2022): 103762.

[30] J. Alshakri, G. J. Hampson, C. Jacquemyn, et al., "A Screening Assessment of the Impact of Sedimentological Heterogeneity on CO_2 Migration and Stratigraphic-Baffling Potential: Sherwood and Bunter Sandstones, UK," in *Geological Society of London*, vol. 528 of *Enabling Secure Subsurface Storage in Future Energy Systems*, (Special Publication, 2023): 245–266.

[31] S. Deng, R. Zhao, Q. Kong, Y. Li, and B. Li, "Two Distinct Strike-Slip Fault Networks in the Shunbei Area and Its Surroundings, Tarim Basin: Hydrocarbon Accumulation, Distribution, and Controlling Factors," *AAPG Bulletin* 106, no. 1 (2022): 77–102.

[32] F. Jiao, "Significance of Oil and Gas Exploration in NE Strike-Slip Fault Belts in Shuntuoguole Area of Tarim Basin," *Oil & Gas Geology* 38 (2017): 831–839.

[33] D. Zhu, Q. Liu, J. Zhang, Q. Ding, Z. He, and X. Zhang, "Types of Fluid Alteration and Developing Mechanism of Deep Marine Carbonate Reservoirs," *Geofluids* 2019 (2019): 3630915.

[34] C. Lin, H. Yang, J. Liu, et al., "Sequence Architecture and Depositional Evolution of the Ordovician Carbonate Platform Margins in the Tarim Basin and Its Response to Tectonism and Sea-Level Change," *Basin Research* 24, no. 5 (2012): 559–582.

[35] D. He, C. Jia, D. Li, C. Zhang, Q. Meng, and X. Shi, "Formation and Evolution of Polycyclic Superimposed Tarim Basin," *Oil & Gas Geology* 26 (2005): 64–77.

[36] S. Deng, H. Li, Z. Zhang, J. Zhang, and X. Yang, "Structural Characterization of Intracratonic Strike-Slip Faults in the Central Tarim Basin," *AAPG Bulletin* 103, no. 1 (2019): 109–137.

[37] Y. Wang, H. Chen, H. Guo, et al., "Hydrocarbon Charging History of the Ultra-Deep Reservoir in Shun 1 Strike-Slip Fault Zone, Tarim Basin," *Oil & Gas Geology* 40 (2019): 972–989.

[38] X. Dong, G. J. Hampson, L. Lonergan, and Y. Wang, "Seismic Attribute-Driven Analysis of an Ultra-Deep Carbonate Reservoir: Middle Cambrian to Middle Ordovician Strata, North-Central Tarim Basin, Northwest China," *Journal of Sedimentary Research* 94, no. 6 (2024): 871–894.

[39] S. Yang, H. Chen, Z. Li, et al., "Early Permian Tarim Large Igneous Province in Northwest China," *Science China Earth Sciences* 56, no. 12 (2013): 2015–2026.

[40] Y.-G. Xu, X. Wei, Z.-Y. Luo, H.-Q. Liu, and J. Cao, "The Early Permian Tarim Large Igneous Province: Main Characteristics and a Plume Incubation Model," *Lithos* 204 (2014): 20–35.

[41] D. Y. Zhu, Z. J. Jin, and W. X. Hu, "Hydrothermal Recrystallization of the Lower Ordovician Dolomite and Its Significance to Reservoir in Northern Tarim Basin," *Science China Earth Sciences* 53, no. 3 (2010): 368–381.

[42] S. Dong, D. Chen, H. Qing, et al., "Hydrothermal Alteration of Dolostones in the Lower Ordovician, Tarim Basin, NW China: Multiple Constraints From Petrology, Isotope Geochemistry and Fluid Inclusion Microthermometry," *Marine and Petroleum Geology* 46 (2013): 270–286.

[43] Y. Kang and Z. Kang, "Tectonic Evolution and Oil and Gas of Tarim Basin," *Journal of Southeast Asian Earth Sciences* 3 (1996): 317–325.

[44] D. Li, D. Liang, C. Jia, G. Wang, Q. Wu, and D. He, "Hydrocarbon Accumulations in the Tarim Basin, China," *AAPG Bulletin* 80 (1996): 1587–1603.

[45] C. Jia and G. Wei, "Structural Characteristics and Petroliferous Features of Tarim Basin," *Chinese Science Bulletin* 47, no. S1 (2002): 1–11.

[46] Z. Gao, Q. Ding, and X. Hu, "Characteristics and Controlling Factors of Carbonate Intra-Platform Shoals in the Tarim Basin, NW China," *Journal of Petroleum Science and Engineering* 127 (2015): 20–34.

[47] X. Yan, T. Li, and T. Zhang, "Ordovician Basement Hydrocarbon Reservoirs in the Tarim Basin, China," *Acta Geologica Sinica—English Edition* 78, no. 3 (2004): 676–683.
[48] X. Pang, J. Tian, H. Pang, C. Xiang, Z. Jiang, and S. Li, "Main Progress and Problems in Research on Ordovician Hydrocarbon Accumulation in the Tarim Basin," *Petroleum Science* 7, no. 2 (2010): 147–163.
[49] M. Meng and T. Fan, "Sedimentary Characteristics and Formation Mechanisms of the Ordovician Carbonate Shoals in the Tarim Basin, NW China," *Carbonates and Evaporites* 35, no. 3 (2020): 1–18.
[50] L. Qi, "Oil and Gas Breakthrough in Ultra-Deep Ordovician Carbonate Formations in Shuntuoguole Uplift, Tarim Basin," *China Petroleum Exploration* 21 (2016): 38–51.
[51] Q. Sun, T. Fan, Z. Gao, et al., "New Insights on the Geometry and Kinematics of the Shunbei 5 Strike-Slip Fault in the Central Tarim Basin, China," *Journal of Structural Geology* 150 (2021): 104400.
[52] G. Zhu, K. Zhao, H. Yu, F. Huang, and T. Li, "Silicon Isotopic Constraints on the Genesis of Cherts in the Ordovician Sedimentary Succession in Tarim Basin, Western China," *Journal of Asian Earth Sciences* 215 (2021): 104795.
[53] K. Shang, H. Lyu, Z. Cao, J. Han, W. Gong, and C. Huang, "Distribution and Significance of Middle Ordovician Yijianfang Formation in Shuntuoguole Lower Uplift, Tarim Basin," *Petroleum Geology & Experiment* 40 (2018): 353–361.
[54] J. Yu, K. Shi, Q. Wang, et al., "Structural Diagenesis of Deep Carbonate Rocks Controlled by Intra-Cratonic Strike-Slip Faulting: An Example in the Shunbei Area of the Tarim Basin, NW China," *Basin Research* 34, no. 5 (2022): 1601–1631.
[55] X. Lu, Y. Wang, F. Tian, et al., "New Insights Into the Carbonate Karstic Fault System and Reservoir Formation in the Southern Tahe Area of the Tarim Basin," *Marine and Petroleum Geology* 86 (2017): 587–605.
[56] Y. Zhu, Y. Zhang, X. Zhao, et al., "The Fault Effects on the Oil Migration in the Ultra-Deep Fuman Oilfield of the Tarim Basin, NW China," *Energies* 15, no. 16 (2022): 5789.
[57] C. Xiong, Z. Cai, B. Ma, et al., "Control of Strike-Slip Faults on Condensate Gas Accumulation and Enrichment in the Ordovician Carbonate Reservoirs of the Central Tarim Basin, NW China," *Journal of Asian Earth Sciences* 263 (2024): 106019.
[58] D.-B. Ma, G.-H. Wu, N. Scarselli, X.-S. Luo, J.-F. Han, and Z.-Y. Chen, "Seismic Damage Zone and Width-Throw Scaling along the Strike-Slip Faults in the Ordovician Carbonates in the Tarim Basin," *Petroleum Science* 16, no. 4 (2019): 752–762.
[59] G. Wu, L. Gao, Y. Zhang, C. Ning, and E. Xie, "Fracture Attributes in Reservoir-Scale Carbonate Fault Damage Zones and Implications for Damage Zone Width and Growth in the Deep Subsurface," *Journal of Structural Geology* 118 (2019): 181–193.
[60] Y. Zhao, G. Wu, Y. Zhang, et al., "The Strike-Slip Fault Effects on Tight Ordovician Reef-Shoal Reservoirs in the Central Tarim Basin (NW China)," *Energies* 16, no. 6 (2023): 2575.
[61] Q. Sun, T. Fan, R. E. Holdsworth, et al., "The Spatial Characterization of Stepovers Along Deeply-Buried Strike-Slip Faults and Their Influence on Reservoir Distribution in the Central Tarim Basin, NW China," *Journal of Structural Geology* 170 (2023): 104849.
[62] L. Yun and S. Deng, "Structural Styles of Deep Strike-Slip Faults in Tarim Basin and the Characteristics of Their Control on Reservoir Formation and Hydrocarbon Accumulation: A Case Study of Shunbei Oil and Gas Field," *Acta Petrolei Sinica* 43 (2022): 770–787.
[63] B. Liu, L. Qi, Z. Li, et al., "Spatial Characterization and Quantitative Description Technology for Ultra-Deep Fault-Karst Reservoirs in the Shunbei Area," *Acta Petrolei Sinica* 41 (2020): 412.
[64] J. Su, X. Wang, H. Yang, et al., "Hydrothermal Alteration and Hydrocarbon Accumulations in Ultra-Deep Carbonate Reservoirs along a Strike-Slip Fault System, Tarim Basin, NW China," *Journal of Petroleum Science and Engineering* 203 (2021): 108605.
[65] G. Song, H. Li, N. Ye, et al., "Types and Features of Diagenetic Fluids in Shunbei No. 4 Strike-Slip Fault Zone in Shuntuoguole Low Uplift, Tarim Basin," *Petroleum Geology & Experiment* 44 (2022): 603–612.
[66] V. Baqués, E. Ukar, S. E. Laubach, S. R. Forstner, and A. Fall, "Fracture, Dissolution, and Cementation Events in Ordovician Carbonate Reservoirs, Tarim Basin, NW China," *Geofluids* 2020 (2020): 1–28.
[67] B. Jiu, W. Huang, N. Mu, and M. He, "Effect of Hydrothermal Fluids on the Ultra-Deep Ordovician Carbonate Rocks in Tarim Basin, China," *Journal of Petroleum Science and Engineering* 194 (2020): 107445.
[68] B. Li and K. Goldberg, "Diagenesis and Reservoir Quality of Cambrian Carbonates in the Tarim Basin, Northwestern China," *Journal of Asian Earth Sciences* 223 (2022): 104972.
[69] B. Jiu, W. Huang, N. Mu, and R. Hao, "Petrology, Mineralogy and Geochemistry of Ordovician Rocks in the Southwest of Tarim Basin, Implications for Genetic Mechanism and Evolution Model of the Hydrothermal Reformed-Paleokarst Carbonate Reservoir," *Marine and Petroleum Geology* 140 (2022): 105687.
[70] G. Wu, E. Xie, Y. Zhang, H. Qing, X. Luo, and C. Sun, "Structural Diagenesis in Carbonate Rocks as Identified in Fault Damage Zones in the Northern Tarim Basin, NW China," *Minerals* 9, no. 6 (2019): 360.
[71] G. Box, W. Hunter, and J. Hunter, *Statistics for Experimenters: an Introduction to Design, Data Analysis, and Model Building* (Wiley Press, New York, USA, 1978).
[72] E. Damsleth, A. Hage, and R. Volden, "Maximum Information at Minimum Cost: A North Sea Field Development Study With An Experimental Design," *Journal of Petroleum Technology* 44, no. 12 (1992): 1350–1356.
[73] C. D. White and S. A. Royer, "Experimental Design as a Framework for Reservoir Studies," in *SPE Reservoir Simulation Symposium*, (Houston, Texas, USA: One Petro, 2003).
[74] Z. Zhao, J. Liu, W. Ding, R. Yang, and G. Zhao, "Analysis of Seismic Damage Zones: A Case Study of the Ordovician Formation in the Shunbei 5 Fault Zone, Tarim Basin, China," *Journal of Marine Science and Engineering* 9, no. 6 (2021): 630.
[75] R. J. Knipe, "Faulting Processes and Fault Seal, Structural and Tectonic Modelling and Its Application to Petroleum Geology," in *Norwegian Petroleum Society*, 1, (Special Publication, 1992): 325–342.
[76] J. S. Caine, J. P. Evans, and C. B. Forster, "Fault Zone Architecture and Permeability Structure," *Geology* 24, no. 11 (1996): 1025–1028.
[77] M. Antonellini, E. Tondi, F. Agosta, A. Aydin, and G. Cello, "Failure Modes in Deep-Water Carbonates and Their Impact for Fault Development: Majella Mountain, Central Apennines, Italy," *Marine and Petroleum Geology* 25, no. 10 (2008): 1074–1096.

[78] J.-M. Questiaux, G. D. Couples, and N. Ruby, "Fractured Reservoirs With Fracture Corridors," *Geophysical Prospecting* 58, no. 2 (2010): 279–295.
[79] Z. Wang, Z. Gao, T. Fan, H. Zhang, L. Qi, and L. Yun, "Hydrocarbon-Bearing Characteristics of the SB1 Strike-Slip Fault Zone in the North of the Shuntuo Low Uplift, Tarim Basin," *Petroleum Geoscience* 27, no. 1 (2021): petgeo2019-144.
[80] L. Micarelli, A. Benedicto, and C. A. J. Wibberley, "Structural Evolution and Permeability of Normal Fault Zones in Highly Porous Carbonate Rocks," *Journal of Structural Geology* 28, no. 7 (2006): 1214–1227.
[81] M. E. J. Wilson, M. J. Evans, N. H. Oxtoby, D. S. Nas, T. Donnelly, and M. Thirlwall, "Reservoir Quality, Textural Evolution, and Origin of Fault-Associated Dolomites," *AAPG Bulletin* 91, no. 9 (2007): 1247–1272.
[82] Y.-S. Kim, D. C. P. Peacock, and D. J. Sanderson, "Fault Damage Zones," *Journal of Structural Geology* 26, no. 3 (2004): 503–517.
[83] A. Lin and K. Yamashita, "Spatial Variations in Damage Zone Width along Strike-Slip Faults: An Example from Active Faults in Southwest Japan," *Journal of Structural Geology* 57 (2013): 1–15.
[84] T. P. Harding, "Seismic Characteristics and Identification of Negative Flower Structures, Positive Flower Structures, and Positive Structural Inversion," *AAPG Bulletin* 69 (1985): 582–600.
[85] Y. Zhang, Q. Mao, H. Li, Z. Li, J. Han, and B. Lin, "Characteristics and Practical Application of Ultra-Deep Fault-Controlled Fractured Cavity Type Reservoir in Central Shunbei Area," *China Petroleum Exploration* 28 (2023): 1–13.
[86] Z. Shen, Y. Neng, J. Han, et al., "Structural Styles and Linkage Evolution in the Middle Segment of a Strike-Slip Fault: A Case from the Tarim Basin, NW China," *Journal of Structural Geology* 157 (2022): 104558.
[87] Y. Liu, J. Suppe, Y. Cao, et al., "Linkage and Formation of Strike-Slip Faults in Deep Basins and the Implications for Petroleum Accumulation: A Case Study from the Shunbei Area of the Tarim Basin, China," *AAPG Bulletin* 107 (2023): 331–355.
[88] A. Billi, "Grain Size Distribution and Thickness of Breccia and Gouge Zones From Thin (<1m) Strike-Slip Fault Cores in Limestone," *Journal of Structural Geology* 27 (2005): 1823–1837.
[89] E. A. H. Michie, I. Kaminskaite, A. P. Cooke, Q. J. Fisher, G. Yielding, and S. D. Tobiss, "Along-Strike Permeability Variation in Carbonate-Hosted Fault Zones," *Journal of Structural Geology* 142 (2021): 104236.
[90] T. J. Haines, E. A. H. Michie, J. E. Neilson, and D. Healy, "Permeability Evolution across Carbonate Hosted Normal Fault Zones," *Marine and Petroleum Geology* 72 (2016): 62–82.
[91] A. Ebert, M. Herwegh, B. Evans, A. Pfiffner, N. Austin, and T. Vennemann, "Microfabrics in Carbonate Mylonites along a Large-Scale Shear Zone (Helvetic Alps)," *Tectonophysics* 444 (2007): 1–26.
[92] A. Billi, F. Salvini, and F. Storti, "The Damage Zone-Fault Core Transition in Carbonate Rocks: Implications for Fault Growth, Structure and Permeability," *Journal of Structural Geology* 25, no. 11 (2003): 1779–1794.
[93] P. Jeanne, Y. Guglielmi, J. Lamarche, F. Cappa, and L. Marié, "Architectural Characteristics and Petrophysical Properties Evolution of a Strike-Slip Fault Zone in a Fractured Porous Carbonate Reservoir," *Journal of Structural Geology* 44 (2012): 93–109.
[94] F. Geng, H. Wang, J. Hao, and P. Gao, "Internal Structure Characteristics and Formation Mechanism of Reverse Fault in the Carbonate Rock, A Case Study of Outcrops in Xike'er Area, Tarim Basin, Northwest China," *Frontiers in Earth Science* 9 (2021): 793016.
[95] T. Zhao, R. Zhao, Q. Kong, C. Xiao, and H. Lin, "Analysis of Water-Rock Interaction in Middle-Lower Ordovician Strike-Slip Fault in T-SH Oilfield, Tarim Basin, NW China," *Carbonates and Evaporites* 37, no. 3 (2022): 42.
[96] L. Jiang, A. Shen, Z. Qiao, et al., "Hypogenic Karstic Cavities Formed by Tectonic-Driven Fluid Mixing in the Ordovician Carbonates From the Tarim Basin, Northwestern China," *AAPG Bulletin* 108, no. 1 (2024): 159–178.
[97] L. Chen, H. Zhang, Z. Cai, F. Hao, Y. Xue, and W. Zhao, "Petrographic, Mineralogical and Geochemical Constraints on the Fluid Origin and Multistage Karstification of the Middle-Lower Ordovician Carbonate Reservoir, NW Tarim Basin, China," *Journal of Petroleum Science and Engineering* 208 (2022): 109561.
[98] N. Ye, Y. Li, B. Huang, et al., "Hydrothermal Silicification and Its Impact on Lower-Middle Ordovician Carbonates in Shunnan Area, Tarim Basin, NW China," *Geological Journal* 57, no. 9 (2022): 3538–3557.
[99] L. Jia, C. Cai, K. Li, L. Liu, Z. Chen, and X. Tan, "Impact of Fluorine-Bearing Hydrothermal Fluid on Deep Burial Carbonate Reservoirs: A Case Study From the Tazhong Area of Tarim Basin, Northwest China," *Marine and Petroleum Geology* 139 (2022): 105579.
[100] J. Scibek, "Multidisciplinary Database of Permeability of Fault Zones and Surrounding Protolith Rocks at World-Wide Sites," *Scientific Data* 7, no. 1 (2020): 95.
[101] A. Aydin and J. G. Berryman, "Analysis of the Growth of Strike-Slip Faults Using Effective Medium Theory," *Journal of Structural Geology* 32, no. 11 (2010): 1629–1642.
[102] G. de Joussineau, "The Geometrical Properties of Fracture Corridors," *Tectonophysics* 846 (2023): 229637.
[103] Y. Li, J. Sun, H. Wei, and S. Song, "Architectural Features of Fault-Controlled Karst Reservoirs in the Tahe Oilfield," *Journal of Petroleum Science and Engineering* 181 (2019): 106208.
[104] L. Qi, "Characteristics and Inspiration of Ultra-Deep Fault-Karst Reservoir in the Shunbei Area of the Tarim Basin," *China Petroleum Exploration* 25 (2020): 102.
[105] A. Braathen, J. Tveranger, H. Fossen, et al., "Fault Facies and Its Application to Sandstone Reservoirs," *AAPG Bulletin* 93, no. 7 (2009): 891–917.
[106] M. Bentley and S. Smith, "Scenario-Based Reservoir Modelling: the Need for More Determinism and less Anchoring, The Future of Geological Modelling in Hydrocarbon Development," in *Geological Society of London*, 309, (Special Publication, 2008): 145–159.
[107] M. Shahvali, B. Mallison, K. Wei, and H. Gross, "An Alternative to Streamlines for Flow Diagnostics on Structured and Unstructured Grids," *SPE Journal* 17, no. 3 (2012): 768–778.
[108] O. Møyner, S. Krogstad, and K.-A. Lie, "The Application of Flow Diagnostics for Reservoir Management," *SPE Journal* 20, no. 2 (2014): 306–323.
[109] S. Tao, Y. Xu, N. Zou, X. Du, and Y. Hao, "Productivity Prediction of Fractured-Vuggy Reservoirs Under Time-Varied

Flow Rates and Bottom Hole Flow Pressures," *Geofluids* 2022 (2022): 7160747.

[110] J. Bian, D. Hou, Y. Cui, and X. Zhu, "Geochemical Characteristics and Origin of the Ultra-Deep Hydrocarbons From the Shunbei Oilfield in the Tarim Basin, China: Insight From Molecular Biomarkers and Carbon Isotope Geochemistry," *Marine and Petroleum Geology* 158 (2023): 106542.

[111] R. Zhao, T. Zhao, Q. Kong, S. Deng, and H. Li, "Relationship Between Fractures, Stress, Strike-Slip Fault and Reservoir Productivity, China Shunbei Oil Field, Tarim Basin," *Carbonates and Evaporites* 35, no. 3 (2020): 1–14.

[112] R. A. Nelson, *Geologic Analysis of Naturally Fractured Reservoirs* (Gulf Professional Publishing, Houston, Texas, USA, 1985).

[113] J. Allan and S. Q. Sun, "Controls on Recovery Factor in Fractured Reservoirs: Lessons Learned From 100 Fractured Fields," in *SPE Paper 84590, Presented at SPE Annual Technical Conference and Exhibition*, (Denver, Colorado, USA: One Petro, 2003).

[114] L. Yun, "Controlling Effect of NE Strike Slip Fault System on Reservoir Development and Hydrocarbon Accumulation and Its Geological Significance in the Eastern Shunbei Area, Tarim Basin," *China Petroleum Exploration* 26 (2021): 41–52.

[115] X. Lu, Y. Wang, D. Yang, and X. Wang, "Characterization of Paleo-Karst Reservoir and Faulted Karst Reservoir in Tahe Oilfield, Tarim Basin, China," *Advances in Geo-Energy Research* 4, no. 3 (2020): 339–348.

[116] M. C. Baddeley, A. Curtis, and R. Wood, "An Introduction to Prior Information Derived From Probabilistic Judgements: Elicitation of Knowledge, Cognitive Bias and Herding," in *Geological Society of London*, vol. 239 of *Geological Prior Information: Informing Science and Engineering*, (Special Publication, 2004): 15–27.

[117] D. Polson and A. Curtis, "Dynamics of Uncertainty in Geological Interpretation," *Journal of the Geological Society of London* 167, no. 1 (2010): 5–10.

[118] D. Polson, A. Curtis, and C. Vivalda, "The Evolving Perception of Risk During Reservoir Evaluation Projects for Geological Storage of CO_2," *International Journal of Greenhouse Gas Control* 9 (2012): 10–23.

[119] C. H. Randle, C. E. Bond, R. M. Lark, and A. A. Monaghan, "Uncertainty in Geological Interpretations: Effectiveness of Expert Elicitations," *Geosphere* 15, no. 1 (2019): 108–118.